AD NUMBER
AD820563
LIMITATION CHANGES

TO:

Approved for public release; distribution is unlimited.

FROM:

Distribution authorized to U.S. Gov't. agencies and their contractors; Administrative/Operational Use; 23 SEP 1967. Other requests shall be referred to Air Force Cambridge Research Laboratory, Hanscom AFB, MA.

AUTHORITY

AFCRL ltr dtd 22 Dec 1971

THEORETICAL STUDY OF MAGNETOHYDRODYNAMIC WAVE PROPAGATION

and

EXPERIMENTAL STUDY OF COLLISIONAL EFFECTS ON WAVE PROPAGATION

by

Sheldon L. Kahalas
Brian L. Murphy
James C. Woo

MT. AUBURN RESEARCH ASSOCIATES, INC.
12 Norfolk Street
Cambridge, Massachusetts 02139

Annual Report
covering period
24 August 1966 - 23 August 1967

23 September 1967

ABSTRACT

Two problems relevant to the magnetotelluric detection
of high altitude nuclear detonations are treated in this report:

(1) A computer program is described for solving the poloidal
magnetohydrodynamic wave equation with a source current present
in a realistic though axisymmetric model of the outer ionosphere.
Arguments are given that the poloidal mode of the axisymmetric
model should produce the relevant features of a more realistic
asymmetric model.

(2) The effects of collisions on the propagation of the
wave signal through the lower ionosphere is studied experimentally
in a laboratory plasma. The facilities constructed for the
purpose and the experimental program are described in this report.

TABLE OF CONTENTS

A. Theoretical Study of Magnetohydrodynamic Wave Propagation

1. Introduction

This work has been sponsored by the Advanced Research Projects Agency under the Nuclear Test Detection Program. The magnetotelluric detection of high altitude nuclear detonations is far less advanced than many other detection methods. One of the primary reasons for this is that a complete theoretical understanding of the propagation of a magnetic disturbance in the ionosphere is lacking.

This is the subject of the present theoretical study. We are concerned with the radiation of magnetohydrodynamic waves by a current source located within the ionospheric cavity surrounding the earth.

In particular, we treat only the poloidal or isotropic mode which is uncoupled from the toroidal or guided mode for an axisymmetric geometry. This simplification originates, of course, in the interests of tractability, but some recent studies, described in section 2, indicate that the amplitude of the guided mode is generally several orders of magnitude smaller than that of the isotropic mode if the ionospheric medium is not too highly asymmetric.

The problem we are treating, then, is an ordinary waveguide problem, but for a realistic variation of the ionospheric parameters (ambient ion density and magnetic field strength) it is still not amenable to analytic solution and the wave equation must be solved numerically. This computation using the method of lines (straight-line method), attributed to M. G. Slobodyanskii[1], is described in section 4.

-1-

First, however, in section 3 we solve the poloidal wave
equation analytically for the special (and unrealistic) case in
which the Alfven speed varies linearly with the distance from the
center of the earth. The object here is twofold: (1) We can get
some assurance that the computer program described in section 4 is
working correctly by testing it on this special case. (2) We can
get some feeling for the way in which the orders of magnitude of
the various ionospheric parameters affect the wave propagation.
In particular, the analytic works of section 3 takes the finite
ionospheric conductivity into account.

Finally, in section 5 the analytic and computer studies
are compared for the special case previously mentioned and the
computer results for more realistic ionospheric models are described
and interpreted.

2. Some Recent Developments in the Theory of Magnetohydrodynamic Wave Propagation

The calculational work has dealt with solving the axisymmetric poloidal equation. While consideration of this special case certainly does not yield a complete description of magnetohydrodynamic wave propagation, there are good arguments as to why this case is an important element of any such description.

The basic magnetohydrodynamic equations are given in section 3. If the assumption is made that the field amplitudes are independent of φ, then the magnetohydrodynamic wave equation breaks up into two independent equations. One of these describes the poloidal mode which will be treated in more detail below. The second is the toroidal mode which has properties making it similar to the guided mode for plane wave propagation in a constant density medium with infinite conductivity and a constant magnetic field.

For the toroidal mode in a dipole field, the equations are

$$4\pi \rho_{10} \frac{\partial v_\varphi}{\partial t} = \left[\underset{\sim}{B_0} \cdot \nabla - \frac{3M\cos\theta}{r^4} \right] b_\varphi \tag{2.1}$$

and

$$\frac{\partial b_\varphi}{\partial t} = \left[\underset{\sim}{B_0} \cdot \nabla + \frac{3M\cos\theta}{r^4} \right] v_\varphi \tag{2.2}$$

Since $\underset{\sim}{B}_0 \cdot \nabla$ is the only operator present in these equations,
a change of variable is suggested from r, θ to ν, θ where $\nu \equiv \sin^2\theta/r$.
With $\mu \equiv \cos \theta$, these equations become

$$4\pi\rho_c \frac{\partial v_\varphi}{\partial t} = \left(M\nu^4/\sin^9\theta\right)\left(\frac{\partial}{\partial \mu} \sin^3 b_\varphi\right)_\nu \qquad (2.3)$$

and

$$\frac{\partial b_\varphi}{\partial t} = \left(M\nu^4/\sin^3\theta\right)\left(\frac{\partial}{\partial \mu} \frac{v_\varphi}{\sin^3\theta}\right)_\nu$$

$$(2.4)$$

Defining $g(\mu,\nu) = v_\varphi/\sin^3\theta$ and $\beta^2(\mu,\nu) = 4\pi\rho_0(1-\mu^2)^6/(M\nu^4)^2$ the
toroidal equation has the form

$$\left(\frac{\partial^2 g}{\partial \mu^2}\right)_\nu = \beta^2(\mu,\nu) \frac{\partial^2 g}{\partial t^2} \qquad (2.5)$$

From this equation, it is easily seen that the eigenvalues arising
in the solution of any boundary value problem are functions of ν,
since $\left(\dfrac{\partial^2 g}{\partial\mu^2}\right)_\nu$ denotes the second derivative of g with respect to
μ with ν being held constant. Since $\nu \equiv \sin^2\theta/r$ is a function of the
spatial coordinates and is essentially a parameter which labels
different geomagnetic lines of force, we have the unusual situation
that, for toroidal axisymmetric wave disturbances, the eigenvalues are
a function of position.

This condition has been discussed by Radrski and McClay[3]. In carrying out an analysis using a simplified geometry, they note that the charge density and the current density parallel to the magnetic field lines are both proportional to derivatives with respect to ν of field quantities. Now the field quantities vary in time as $e^{i\omega t}$ where $\omega = \omega(\nu)$ from Eq. (2.5). Thus we have a situation where the charge and parallel current densities vary as $\frac{\partial \omega}{\partial \nu} t$, that is,

they grow indefinitely with time. This contradicts, among other things, the initial assumption that all quantities vary as $e^{i\omega t}$. Thus one must conclude that under the hydromagnetic approximation, the toroidal field must be zero. Stated differently, in order for the eigenvalues of the toroidal mode to depend on the cavity size, rather than on the label ν of a particular magnetic field line, it is necessary to introduce into Eq. (2.5) derivatives with respect to ν, so that the toroidal field amplitude is coupled across field lines. Once this is done, however, the simple model of Alfven waves propagating along geomagnetic field lines and perhaps bouncing back and forth between conjugate points with a characteristic bounce period must also be laid to rest.

One means of introducing derivatives with respect to ν in (2.5) is to allow the presence of a finite electric field parallel to the magnetic lines of force, that is, change the simple equation

$$\underset{\sim}{E} = -\frac{1}{c} \underset{\sim}{v} \times \underset{\sim}{B_c} \tag{2.6}$$

to allow for other effects such as Hall effect, electron pressure, finite conductivity, etc. If the Hall effect is introduced, so that a parallel electric field component is introduced, it may be shown[3]

-5-

that the poloidal field is not changed, but that the toroidal fie_d
is coupled to the poloidal field and that the toroidal field vanishes
in the limit of the hydromagnetic approximation. Also for geophysical
parameters, the toroidal field is small compared with the poloidal
field.

Thus we are led to conclude for axisymmetric magnetohydro-
dynamic wave propagation that it is the poloidal mode which is
important.

The axisymmetric poloidal and toroidal modes are the $m = 0$
modes which result when the field amplitudes are assumed to vary as
$e^{im\varphi}$ (where m is an integer and φ is the third coordinate of the
usual (r, θ, φ) spherical coordinate system). The higher order modes
such as $m = 1, 2$, etc. cannot be so easily neglected. However, one
can make two statements about the higher order modes:

1. Generally speaking, unless a particular symmetry is
specifically picked out by the nature of the physical problem,
modes with smaller values of m will be more important than modes with
larger values of m.

2. Starting with the magnetohydrodynamic wave equation
for propagation in a dipole field, Dungey[4] has shown that in the
limit of large values of m (i.e., for high azimuthal asymmetry)
there is only one mode propagating. This mode has the same field
variables describing it as does the $m = 0$ poloidal mode. On the
other hand, as already indicated, for m large the field amplitudes
which described the toroidal mode for $m = 0$ are small. A further
very important property of the surviving mode in the large m case is
that its wave equation has a form quite similar to Eq. (2.5). In
particular, the wave amplitude in the highly asymmetric case do not
depend, to a first approximation, on derivatives perpendicular to
the magnetic field lines. Thus, the eigenfrequencies depend upon

spatial coordinates as before. Since this leads to an unstable growth of the mode we are led to conclude that these modes have near-zero amplitude in a first approximation[5].

From this we are led to believe that the $m = 0$ poloidal mode whose equation we have solved numerically, and the other low order modes are dominant in problems of magnetohydrodynamic waves propagation in a dipole field in the vicinity of a spherical earth.

3. Analytic Solution of the Poloidal Magnetohydrodynamic Wave Equation with Finite Atmospheric Conductivity for a Special Case

The basic equations are as given in a previous report[6] with the addition of a finite scalar conductivity.

$$\nabla \times \underset{\sim}{B} = \frac{4\pi}{c}\left(\underset{\sim}{J} + \underset{\sim}{\dot{\jmath}}\right)$$

$$\tag{3-1}$$

$$\nabla \times \underset{\sim}{E} = -\frac{1}{c}\frac{\partial \underset{\sim}{B}}{\partial t}$$

$$\tag{3-2}$$

$$\underset{\sim}{E} = \frac{\underset{\sim}{\dot{\jmath}}}{\sigma} - \frac{\underset{\sim}{V}}{c} \times \underset{\sim}{B_o}$$

$$\tag{3-3}$$

$$S_o \frac{d\underset{\sim}{V}}{dt} = \frac{\underset{\sim}{\dot{\jmath}}}{c} \times \underset{\sim}{B_o}$$

$$\tag{3-4}$$

From (3-1) and (3-2):

$$\nabla \times \nabla \times \underset{\sim}{E} = -\frac{1}{c}\frac{\partial}{\partial t}\left(\nabla \times \underset{\sim}{B}\right) = -\frac{4\pi}{c^2}\frac{\partial}{\partial t}\left(\underset{\sim}{J} + \underset{\sim}{\dot{\jmath}}\right) \tag{3-5}$$

or using (3-4) and (3-3)

$$\underset{\sim}{B_o} \times \underset{\wedge}{B_o} \times \nabla \times \nabla \times \underset{\sim}{E} + \underset{\sim}{B_o} \times \underset{\sim}{B_o} \times \frac{4\pi}{c^2}\frac{\partial \underset{\sim}{J}}{\partial t}$$

$$= -\frac{4\pi}{c}\frac{\partial}{\partial t}\left[\left(\frac{\underset{\sim}{\dot{\jmath}}}{c} \times \underset{\sim}{B_o}\right) \times \underset{\sim}{B_o}\right] \tag{3-6}$$

$$= -4\pi S_o \frac{d^2}{dt^2}\left(\frac{\underset{\sim}{V}}{c} \times \underset{\sim}{B_o}\right) = -4\pi S_o \frac{d^2}{dt^2}\left(\frac{\underset{\sim}{\dot{\jmath}}}{\sigma} - \underset{\sim}{E}\right)$$

but from (3-5)

$$\frac{\partial \hat{y}}{\partial t} = -\frac{\partial J}{\partial t} - \frac{c^2}{4\pi} \nabla \times \nabla \times \underset{\sim}{E}$$

(3-7)

so that (3-6) becomes:

$$\underset{\sim}{B_0} \times \underset{\sim}{B_0} \times \nabla \times \nabla \times \underset{\sim}{E} + \underset{\sim}{B_0} \times \underset{\sim}{B_0} \times \frac{4\pi}{c^2} \frac{\partial J}{\partial t}$$

$$-4\pi S_0 \frac{\partial^2 \underset{\sim}{E}}{\partial t^2} = -\frac{4\pi S_0}{\sigma} \frac{\partial^2 \underset{\sim}{J}}{\partial t^2}$$

$$= \frac{4\pi S_0}{\sigma} \left(\frac{\partial^2 \underset{\sim}{J}}{\partial t^2} + \frac{c^2}{4\pi} \nabla \times \nabla \times \frac{\partial \underset{\sim}{E}}{\partial t} \right)$$

(3-8)

Taking an $e^{i\omega t}$ time dependence this becomes:

$$\left[\underset{\sim}{B_0} \times \underset{\sim}{B_0} \times - i S_0 \frac{c^2 \omega}{\sigma} \right] \nabla \times \nabla \times \underset{\sim}{E}$$

$$+ 4\pi S_0 \omega^2 \underset{\sim}{E} = -\left[\underset{\sim}{B_0} \times \underset{\sim}{B_0} - i S_0 \frac{c^2 \omega}{\sigma} \right] \frac{4\pi i \omega}{c^2} \underset{\sim}{J}$$

(3-9)

We take $\underset{\sim}{J}$ to have only a $\hat{\varphi}$ component and $\underset{\sim}{B}_0$ to have $\hat{r}$ and $\hat{\theta}$ components. All quantities are assumed φ independent.

Then one solution to (3-9) is $\underset{\sim}{E} = \hat{\rho} E$, where:

$$\nabla^2 E - \frac{E}{r^2(1-x^2)} + \frac{4\pi \rho_0}{B_0^2}\left[1 + \frac{i\omega \rho_0 c^2}{\sigma B_0^2}\right]^{-1} E \qquad (3\text{-}10)$$
$$= \frac{4\pi i \omega}{c^2} J$$

and $x = \cos\theta$.

Introducing the Alfven velocity $V_A = \dfrac{B_0}{\sqrt{4\pi\rho_0}}$ this becomes:

$$\nabla^2 E - \frac{E}{r^2(1-x^2)} + \frac{\omega^2}{V_A^2}\left[1 + \frac{i\omega}{4\pi\sigma}\frac{c^2}{V_A^2}\right]^{-1} E \qquad (3\text{-}11)$$
$$= \frac{4\pi i \omega}{c^2} J$$

or:

$$\left[\frac{\partial}{\partial r}\, r^2 \frac{\partial}{\partial r} + \frac{\partial}{\partial x}(1-x^2)\frac{\partial}{\partial x} - \frac{1}{1-x^2} + \beta\right] E = \frac{4\pi i\omega}{c^2} r^2 J \qquad (3\text{-}12)$$

where:

$$\beta = \frac{\omega^2}{V_A^2}\, r^2\left[1 + \frac{i\omega}{4\pi\sigma}\frac{c^2}{V_A^2}\right] \qquad (3\text{-}13)$$

As a special case we assume $V_A \propto r$ and $\sigma \propto r^{-2}$ so that β is a constant. When $J = 0$ the homogeneous equation is separable and the orthonormal radial and angular eigenfunctions satisfying the boundary conditions $E = 0$; $r = r_1, r_2$; $\theta = 0, \pi$ are found to be:

$$q_\ell(x) = \sqrt{\frac{2\ell+1}{2\ell(\ell+1)}} \; P_\ell'(x)$$

$$h_m(r) = \left[\ln\left(\frac{r_2}{r_1}\right)^{1/2} \right]^{-1/2} r^{-1/2} \sin\left[\frac{m\pi \ln \frac{r}{r_1}}{\ln \frac{r_2}{r_1}} \right] \qquad (3\text{-}14)$$

$$\int_{-1}^{1} q_\ell(x) \, q_\rho(x) \, dx = \delta_{\ell,\rho} \qquad (3\text{-}15)$$

$$\int_{r_1}^{r_2} h_m(r) \, h_q(r) \, dr = \delta_{m,q}$$

The corresponding eigenvalues are:

$$\beta_{\ell,m} = \frac{1}{4} + \left(\frac{m\pi}{\ln \frac{r_2}{r_1}} \right)^2 + \ell(\ell+1) \qquad (3\text{-}16)$$

We take a current density:

$$J = \frac{I}{2\pi r_0^2} \; \delta(r-r_0) \, \delta(x-x_0) \qquad (3\text{-}17)$$

where I is the total current.

The solution to (3-12) is then just the Green's function:

$$E = -\frac{i\omega}{c^2} I \sum_{\ell,m=1}^{\infty} \frac{q_\ell(x_0) h_m(r_0) \; q_\ell(x) h_m(r)}{\beta_{\ell,m} - \beta} \qquad (3\text{-}18)$$

$$= -\frac{2i\omega}{c^2} I \left(\ell n \frac{r_2}{r_1}\right)^{-1} (r_0 r)^{-1/2} \sum_{\ell,m=1}^{\infty} \frac{2\ell+1}{\ell(\ell+1)} \frac{P_\ell'(x_0) P_\ell'(x)}{\left[\frac{1}{4} + \left(\frac{m\pi}{\ell n \frac{r_2}{r_1}}\right)^2 + \ell(\ell+1) - \beta\right]}$$

$$\sin\left(\frac{m\pi \ell n \frac{r_0}{r_1}}{\ell n \frac{r_2}{r_1}}\right) \sin\left(\frac{m\pi \ell n \frac{r}{r_1}}{\ell n \frac{r_2}{r_1}}\right)$$

The ℓ summation can be done with the aid of the following formula from Magnus and Oberhetinger[7] (the m sum could also be done analytically but this does not prove to be useful):

$$P_\nu'(x) P_\nu^{-1}(x') = \pi^{-1} \sin \pi \nu$$

$$\times \sum_{n=1}^{\infty} (-1)^n \left[(\nu-n)^{-1} - (\nu+n+1)^{-1}\right] P_n'(x) P_n^{-1}(x') \tag{3-19}$$

In equation (3-18) we put $\alpha_m = + \sqrt{\beta - \left(\frac{m\pi}{\ell n \frac{r_2}{r_1}}\right)^2}$

so the sum to be done is:

$$\sum_{\ell=1}^{\infty} \frac{2\ell+1}{\ell(\ell+1)} \frac{P_\ell'(x_0) P_\ell'(x)}{\left[(\ell+\frac{1}{2})^2 - \alpha_m^2\right]} \tag{3-20}$$

$$= \sum_{\ell=1}^{\infty} (2\ell+1)(-1)^\ell \frac{P_\ell'(x_0) P_\ell^{-1}(-x)}{\left[\alpha_m^2 - (\ell+\frac{1}{2})^2\right]}$$

where we have used the relations

$$P_\ell'(x) = -(-1)^\ell P_\ell'(-x) \tag{3-21}$$

$$P_\nu'(-x) = \nu(\nu+1) P_\nu^{-1}(-x) \tag{3-22}$$

-12-

In equation (3-19) we put $\nu = -\tfrac{1}{2} + \alpha_m$, $x = x_0$, $x' = -x$, $n = \ell$:

$$P^{1}_{-\frac{1}{2}+\alpha_m}(x_0)\ P^{-1}_{-\frac{1}{2}+\alpha_m}(-x) = \pi^{-1}\sin\pi\nu$$

$$\sum_{\ell=1}^{\infty} (-1)^{\ell}\frac{(2\ell+1)}{[\alpha_m^2-(\ell+\frac{1}{2})^2]}\ P^{1}_{\ell}(x_0)P^{-1}_{\ell}(-x)$$

(3-23)

comparing (3-20) and (3-23):

$$\sum_{\ell=1}^{\infty}\frac{(2\ell+1)}{\ell(\ell+1)}\ \frac{P^{1}_{\ell}(x_0)\ P^{1}_{\ell}(x)}{[(\ell+\frac{1}{2})^2-\alpha_m^2]}$$

(3-24)

$$= \frac{\pi}{\sin(-\frac{1}{2}+\alpha_m)\pi}\ P^{1}_{-\frac{1}{2}+\alpha_m}(x_0)\ P^{-1}_{-\frac{1}{2}+\alpha_m}(-x)$$

$$= \frac{-\pi}{\cos\alpha_m\pi}\ \frac{P^{1}_{-\frac{1}{2}+\alpha_m}(x_0)\ P^{1}_{-\frac{1}{2}+\alpha_m}(-x)}{(\alpha_m^2-\frac{1}{4})}$$

where we have again used (3-22).

Thus we finally obtain from (3-18):

$$E = \frac{2\pi I\omega}{c^2}\ I\left(\ln\frac{r_2}{r_1}\right)^{-1}(r_0 r)^{-\frac{1}{2}}\sum_{m=1}^{\infty}\frac{P^{1}_{-\frac{1}{2}+\alpha_m}(x_0)\ P^{1}_{-\frac{1}{2}+\alpha_m}(-x)}{\cos\alpha_m\pi\,(\alpha_m^2-\frac{1}{4})}$$

(3-25)

$$\sin\left(\frac{m\pi\ln\frac{r_0}{r_1}}{\ln\frac{r_2}{r_1}}\right)\ \sin\left(\frac{m\pi\ln\frac{r}{b}}{\ln\frac{r_2}{r_1}}\right)$$

-13-

The ℓ summation in (3-18) could have been done directly by writing the sum as a contour integral and using the Watson transformation.[6] The sum in (3-25) would then be the so called residue series:

We write $\beta = \beta^r + i\beta^i$ and

$$\alpha_m = \left\{ \left[\beta^r - \left(\frac{m\pi}{\frac{m r_2}{r_1}}\right)^2 \right]^2 + \beta^{i2} \right\}^{1/4} \exp \frac{i}{2} \tan^{-1}\left[\frac{\beta^i}{\beta^r - \left(\frac{m\pi}{\frac{m r_2}{r_1}}\right)^2} \right]$$

$$= (b^2 + a^2)^{1/4} \exp \frac{i}{2} \tan^{-1} \frac{a}{b} \tag{3-26}$$

$$\alpha_m^i = (a^2 + b^2)^{1/4} \sin \frac{1}{2} \tan^{-1} \frac{a}{b}$$

$$= (a^2 + b^2)^{1/4} \left[1 - \frac{\cos \tan^{-1} \frac{a}{b}}{2} \right]^{1/2} \tag{3-27}$$

$$= (a^2 + b^2)^{1/4} \left[\frac{(b^2 + a^2)^{1/2} - b}{2(b^2 + a^2)^{1/2}} \right]^{1/2}$$

$$= \frac{1}{\sqrt{2}} \left[(b^2 + a^2)^{1/2} - b \right]^{1/2}$$

Similarly we find:

$$\alpha_m^r = \frac{1}{\sqrt{2}} \left[(b^2 + a^2)^{1/2} + b \right]^{1/2} \tag{3-28}$$

Now $|\alpha_m|$ is generally a large number because $\lambda = \dfrac{r\omega}{V_A}$ is large. This might not be true for one value of m;

$$m_0 \simeq \left(\frac{\ln \frac{r_2}{r_1}}{\pi}\right)\lambda \quad \text{if} \quad \frac{\omega}{4\pi\sigma}\frac{c^2}{V_A^2} \ll 1$$

, but

this is a special case which can be treated separately.

For $|\alpha_m|$ large:

$$P'_{-\frac{1}{2}+\alpha_m}(x_0) \simeq \frac{\Gamma(\alpha_m+\frac{3}{2})}{\Gamma(\alpha_m+1)}\left(\frac{\pi}{2}\sin\theta_0\right)^{-\frac{1}{2}} \qquad (3\text{-}29)$$

$$\cos\left(\alpha_m\theta_0+\frac{\pi}{4}\right)\cdot$$

$$\simeq \alpha_m^{\frac{1}{2}}\sqrt{\frac{2}{\pi\sin\theta_0}}\cos\left(\alpha_m\theta_0+\frac{\pi}{4}\right)$$

The situation of interest is $\dfrac{\omega}{4\pi\sigma}\dfrac{c^2}{V_A^2} \ll 1$ and since we are

excluding m too close to $\dfrac{\ln \frac{r_2}{r_1}}{\pi}\lambda$ we have $a \ll b$ so that (3-27) and

(3-28) become:

$$\alpha_m^i \simeq \frac{a}{2b^{\frac{1}{2}}} \simeq \frac{\omega}{8\pi\sigma}\frac{c^2}{V_A^2}\ell\,\lambda\left[1-\left(\frac{m\pi}{\lambda\ln\frac{r_2}{r_1}}\right)^2\right]^{-\frac{1}{2}} \qquad (3\text{-}30)$$

$$\alpha_m^r \simeq b^{\frac{1}{2}} \simeq \lambda\left[1-\left(\frac{m\pi}{\lambda\ln\frac{r_2}{r_1}}\right)^2\right]^{\frac{1}{2}} \qquad (3\text{-}31)$$

$$\text{for}\left(\frac{m\pi}{\lambda\ln\frac{r_2}{r_1}}\right)^2 < 1$$

and:

-15-

$$\alpha_m' = \epsilon^{1/2} = \lambda \left[\left(\frac{m\pi}{\lambda \, \ell n \frac{r_2}{r_1}} \right)^2 - 1 \right]^{1/2}$$

$$\tag{3-32}$$

$$\alpha_m^r = \frac{a}{2\epsilon^{1/2}} \simeq \frac{\omega}{4\pi\sigma} \frac{c^2}{V_A^2} \lambda \left[\left(\frac{m\pi}{\lambda \, \ell n \frac{r_2}{r_1}} \right)^2 - 1 \right]^{-1/2}$$

$$\tag{3-33}$$

$$\text{for} \left(\frac{m\pi}{\lambda \, \ell n \frac{r_2}{r_1}} \right)^2 > 1$$

If $(\alpha_m' \theta_0) > 1$ then (3-29) gives:

$$P'_{-1/2 + \alpha_m}(x_0) \simeq \alpha_m'^{1/2} \sqrt{\frac{2}{\pi \sin \theta_0}} \; e^{\alpha_m' \theta_0}$$

$$\tag{3-34}$$

$$[\cos \alpha_m^r \theta_0 - i \sin \alpha_m^r \theta_0]$$

and:

$$\frac{P'_{-1/2 + \alpha_m}(x_0) \, P'_{-1/2 + \alpha_m}(-x)}{\cos \alpha_m \pi \, (\alpha_m^2 - 1/4)}$$

$$\tag{3-35}$$

$$\simeq \frac{2}{\pi \alpha_m \sqrt{\sin \theta_0 \, \sin \theta}} \; e^{-\alpha_m' (\theta - \theta_0)}$$

$$\times [\cos \alpha_m^r \theta_0 - i \sin \alpha_m^r \theta_0]$$
$$\times [\cos \alpha_m^r (\pi - \theta) - i \sin \alpha_m^r (\pi - \theta)]$$
$$\times [\cos \alpha_m^r \pi + i \sin \alpha_m^r \pi]$$
$$= \frac{2}{\pi \alpha_m \sqrt{\sin \theta \, \sin \theta_0}} \; e^{-\alpha_m' (\theta - \theta_0)} [\cos \alpha_m^r (\theta - \theta_0) + i \sin \alpha_m^r (\theta - \theta_0)]$$

Clearly, the only terms of importance for θ not too close to θ_0 in (3-25) are those with the smallest α_m^i. From (3-30) and (3-32) this implies $\left(\dfrac{m\pi}{\lambda \ln \dfrac{r_2}{r_1}}\right)^2 < 1.$

Thus the summation in (3-25) may be truncated at an integer $\bar{m}$ where $\bar{m}$ is the order of $\dfrac{\lambda}{\pi} \ln \dfrac{r_2}{r_1}$.

Putting (3-35) in (3-25) we obtain:

$$E \simeq -\frac{4\omega}{c^2} I \left(\ln \frac{r_2}{r_1}\right)^{-1} (r_0 r)^{-1/2} (\sin\theta \sin\theta_0)^{-1/2}$$

$$\sum_{m=1}^{\bar{m}} \frac{e^{-\alpha_m^i (\theta - \theta_0)}}{\alpha_m^r} \left[\sin \alpha_m^r (\theta - \theta_0) - i \cos \alpha_m^r (\theta - \theta_0)\right] \tag{3-36}$$

$$\sin\left(\frac{m\pi \ln \frac{r_2}{r_1}}{\ln \frac{r_2}{r_1}}\right) \sin\left(\frac{m\pi \ln \frac{r}{r_1}}{\ln \frac{r_2}{r_1}}\right)$$

assuming $1 \ll \alpha_m^i \ll \alpha_m^r$.

The magnetic perturbation at the lower cavity boundary is:

$$|B_\theta| = \left|\frac{ic}{\omega} \nabla \times E\right|_{r=r_1} = \frac{ic}{\omega} \frac{1}{r} \frac{d}{dr}(rE)\Big|_{r=r_1}$$

$$= \frac{4\pi}{c} I \left(\ln \frac{r_2}{r_1}\right)^{-2} r_0^{-1/2} r_1^{-3/2} (\sin\theta \sin\theta_0)^{1/2} \tag{3-37}$$

$$\sum_{m=1}^{\bar{m}} \frac{m\, e^{-\alpha_m^i (\theta - \theta_0)}}{\alpha_m^r} \left[\cos \alpha_m^r (\theta - \theta_0) + i \sin \alpha_m^r (\theta - \theta_0)\right]$$

$$\sin\left(\frac{m\pi \ln \frac{r_2}{r_1}}{\ln \frac{r_2}{r_1}}\right)$$

For a low altitude source $\overline{m} \left(\frac{r_0 - r_1}{r_1} \right) \ll 1$

$$B_\theta = \frac{4\pi^2}{c} I \left(\ln \frac{r_2}{r_1} \right)^{-3} r_0^{-1/2} r_1^{-5/2} (r_0 - r_1)(\sin\theta \sin\theta_0)^{-1/2}$$

$$\sum_{m=1}^{\overline{m}} m^2 \frac{e^{-\alpha_m^i(\theta-\theta_0)}}{\alpha_m^r} \cdot \left[\cos \alpha_m^r (\theta - \theta_0) + i \sin \alpha_m^r(\theta - \theta_0) \right]$$

(3-38)

$$= \frac{4}{c} I \left(\ln \frac{r_2}{r_1} \right)^{-1} r_0^{-1/2} r_1^{-5/2} (r_0 - r_1)(\sin\theta \sin\theta_0)^{-1/2}$$

$$\lambda \sum_{m=1}^{\overline{m}} \frac{x^2}{(1-x^2)^{1/2}} e^{-\frac{\omega}{4\pi\sigma} \frac{c^2}{r_1^2} \lambda [1-x^2]^{-1/2}(\theta - \theta_0)}$$

$$\cos \lambda [1-x^2]^{1/2}(\theta - \theta_0) \quad , \quad x = \left(\frac{m\pi}{\lambda \ln \frac{r_2}{r_1}} \right)$$

The impediment to summing this series is the cos factor for
while $1 - x^2$ may not change appreciably as m goes from 1 to $\overline{m}$,
$\lambda(1 - x^2)^{1/2}$ will. Finally, we note that if σ is small enough the m = 1
term dominates through the exponential.

We defer further consideration of the analytic solution until
after the computer solutions have been treated in the next section. We
will then compare the analytic and computer solutions and indicate
how the orders of magnitude of the actual ionospheric variables are
expected to affect magnetohydrodynamic wave propagation.

For a low altitude source $\bar{m}\pi \left(\frac{r_0 - r_1}{r_1}\right) << 1$

$$B_\theta \doteq \frac{4\pi^2}{c} I \left(\ln \frac{r_2}{r_1}\right)^{-3} r_0^{-1/2} r_1^{-5/2} (r_0 - r_1)(\sin\theta \sin\theta_0)^{-1/2}$$

$$\sum_{m=1}^{\bar{m}} m^2 \frac{e^{-\alpha_m^i (\theta - \theta_0)}}{\alpha_m^r} \left[\cos \alpha_m^r (\theta - \theta_0) + i \sin \alpha_m^r (\theta - \theta_0)\right]$$

(3-38)

$$= \frac{4}{c} I \left(\ln \frac{r_2}{r_1}\right)^{-1} r_0^{-1/2} r_1^{-5/2} (r_0 - r_1)(\sin\sigma \sin\theta_0)^{-1/2}$$

$$\lambda \sum_{m=1}^{\bar{m}} \frac{x^2}{(1-x^2)^{1/2}} e^{-\frac{\omega}{8\pi\sigma} \frac{c^2}{V_A^2} \lambda [1-x^2]^{-1/2} (\theta - \theta_0)}$$

$$\cos \lambda [1-x^2]^{1/2} (\theta - \theta_0) \qquad \nu \, x = \left(\frac{m\pi}{\lambda \ln \frac{r_2}{r_1}}\right)$$

The impediment to summing this series is the cos factor for while $1 - x^2$ may not change appreciably as m goes from 1 to $\bar{m}$, $\lambda(1 - x^2)^{\frac{1}{2}}$ will. Finally, we note that if σ is small enough the m = 1 term dominates through the exponential.

We defer further consideration of the analytic solution until after the computer solutions have been treated in the next section. We will then compare the analytic and computer solutions and indicate how the orders of magnitude of the actual ionospheric variables are expected to affect magnetohydrodynamic wave propagation.

4. Numerical Solution of the Wave Equation

The computer program which we have developed is directed towards solving a simple model incorporating several properties of the actual ionospheric environment: (1) Spherical geometry (2) Dipole Magnetic Field.

For a realistic treatment of magnetohydrodynamic wave propagation, it is not sufficient to use ray tracing procedures or a plane-layered-medium approximation. This is easily seen since the wavelength $\lambda = V_a/f$ where V_a is the Alfven velocity and f is the frequency is the order of 1000 km or greater for $V_a \approx 10^8$ cm/sec and f $\approx$ 1 cps or less. This is the scale over which the geomagnetic field varies as well as the distance for which earth-curvature effects become important. Thus, not only is it important, if one wishes to be realistic, to consider the earth's curvature and the dipole nature of the geomagnetic field, but the magnetohydrodynamic equation must be solved without using a geometrical-optics approximation.

The basic equation is (3-8) with $\sigma = \infty$:

$$\frac{\partial^2 \underset{\sim}{E}}{\partial t^2} - \frac{1}{4\pi \rho_0} \left\{ \underset{\sim}{B_0} \times \left[\underset{\sim}{B_0} \times (\nabla \times \nabla \times \underset{\sim}{E}) \right] \right\} = \frac{1}{\rho_0 c^2} \left[\underset{\sim}{B_0} \times \left(\underset{\sim}{B_0} \times \frac{\partial \underset{\sim}{J}}{\partial t} \right) \right] \quad (4\text{-}1)$$

The geomagnetic field $\underset{\sim}{B_0}$ is taken to be of the form

$$\underset{\sim}{B_0} = \frac{M}{r^3} \left(\hat{r}\, 2\cos\theta + \hat{\theta}\, \sin\theta \right) \quad (4\text{-}2)$$

The equation separates into two independent equations if $\underline{J}$ and $\underline{E}$ are assumed to be independent of φ, (i.e., assuming axial symmetry). One of these equations, for the toroidal mode, has already been discussed. The other equation is (3-12) with $\beta = K^2(r)\, r^2$ where $K^2(r) \equiv 4\pi\rho_0 \dfrac{(r)}{M^2}\, r^6 \omega^2$:

$$\frac{\partial}{\partial r}\left(r^2 \frac{\partial E_\varphi}{\partial r}\right) + \frac{\partial}{\partial x}\left[(1-x^2)\frac{\partial E_\varphi}{\partial x}\right] + \left(\frac{K^2 r^2}{1+3x^2} - \frac{1}{1-x^2}\right) E_\varphi$$

$$= \frac{4\pi\omega}{c^2} r^2\, J_\varphi \tag{4-3}$$

This equation has been solved numerically using the method of lines. In this method the equation is gridded along lines of constant x. Thus, with $E_\varphi(r,x) = E_j(r)$, we have a set of equations

$$E_{j+1}\left[\frac{(1-x_j^2)}{h^2} - \frac{2x_j}{h}\right] + E_{j-1}\left[\frac{(1-x_j^2)}{h^2} + \frac{2x_j}{h}\right]$$

$$+ r^2 \frac{d^2 E_j}{dr^2} + 2r \frac{dE_j}{dr} + E_j\left[\frac{-2(1-x_j^2)}{h^2} + \frac{K^2 r^2}{1+3x_j^2} - \frac{1}{1-x_j^2}\right] \tag{4-4}$$

$$= \frac{4\pi\omega}{c^2} r^2\, J_j(r)$$

where $1 \leq j \leq N + 1$ and $N = 2/h$. h is the step size in x in the angular direction. The boundary conditions $E_1(r) = E_{N+1}(r) = 0$ are imposed since E_φ is zero at $\theta = 0^\circ$ and 180°. The set of equations (4-4) are coupled second order differential equations which must be integrated in r. The boundary conditions $E_j(r_1) = E_j(r_2) = 0$ are imposed at the inner and outer boundaries. The source current J_j we have been using is zero everywhere except on a line of constant x. On this line it is zero except between the radii r_a and r_b, where it is constant. Other sources may, of course, be used.

-20-

The basic problem of solving a set of coupled, ordinary differential equations for a two point problem can be attacked in several different ways. The method used in this report is discussed in the Appendix.

Many of the cases run up to the present involve taking $Kr = constant = \lambda$ and ignoring the $1+3x^2$ (i.e., taking it equal to 1) in Eq. (4-4). The reason for this particular choice, as already pointed out, is that the equation is separable and can be solved analytically. A comparison between the analytical and the numerical solution is made in the next section.

Also, after the computer program, as described, was running an entirely different program was set up, similar to Greenfield's[8] and to Chapman and Bostick's[9] in which the partial differential equation was differenced in two dimensions. A comparison of the results of this program with the one using the method of lines gave excellent agreement. This is another check on the correctness of the program.

5. Numerical Results and Interpretations

We first consider the case in which $\lambda = \dfrac{r\omega}{V_A}$ is a constant and
the conductivity is assumed to be infinite. The bounding radii of the
cavity are 6,520 km (150 km altitude taking r_e = 6370 km) and 19,880 km.
Throughout this section the source current is located on the line
$x = \cos\theta = -.6$ (126° 53') between 6,674 and 6,857 km (304 to 487 km
altitude).

Figures (5-1) through (5-4) show the results for $\lambda = 10$ and
(5-5) through (5-8) for $\lambda = 100$. The scale of the amplitude is
arbitrary and the field is plotted as a function of angle for two
values of constant radius and as a function of radius for two values of
constant angle. The remarks which follow pertain as well to the field
amplitudes for other values of radius and angle which have not been
plotted although they are contained in the computer output.

Unfortunately, obtaining the field as a function of angle
is relatively time consuming since the time varies as the square of
the number of angular points and only linearly with the number of
radial points. This is the resul of gridding along lines of constant x
rather than r as described in section 4. The following figures there-
fore generally give only a sketchy indication of the angular variation
although the radial variation is given in some detail.

Since the wavelength is smaller for $\lambda = 100$ than for $\lambda = 10$
it is not surprising that the $\lambda = 100$ curves are more oscillatory.
The most striking feature of these plots is that the field is nearly
separable. For example the number of nodes in the radial function
is independent of the value of the angle. Separability generally
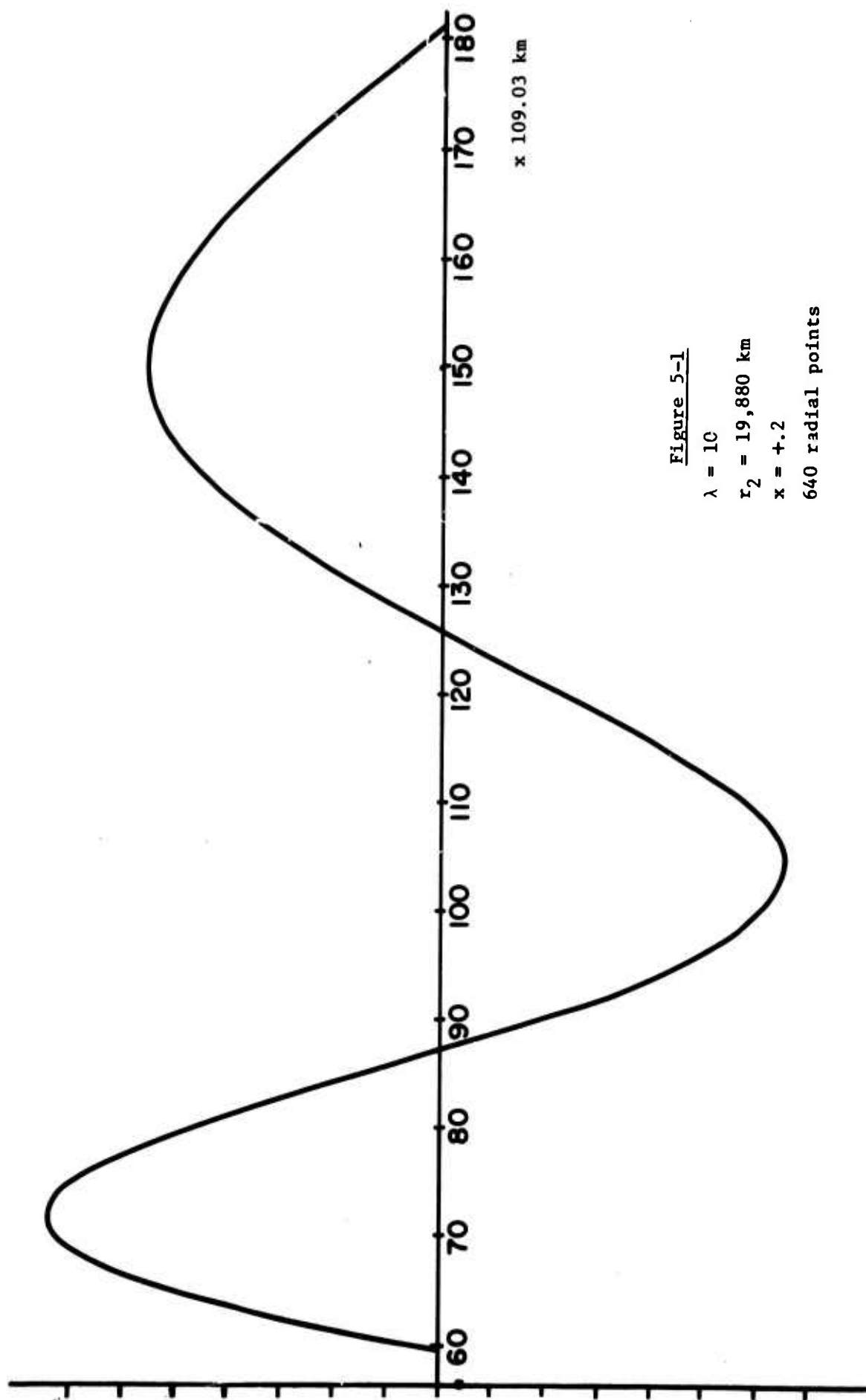seems to be poorest in the vicinity of the source.

5. Numerical Results and Interpretations

We first consider the case in which $\lambda = \dfrac{r\omega}{V_A}$ is a constant and
the conductivity is assumed to be infinite. The bounding radii of the
cavity are 6,520 km (150 km altitude taking r_e = 6370 km) and 19,880 km.
Throughout this section the source current is located on the line
$x = \cos\theta = -.6$ (126° 53') between 6,674 and 6,857 km (304 to 487 km
altitude).

Figures (5-1) through (5-4) show the results for $\lambda = 10$ and
(5-5) through (5-8) for $\lambda = 100$. The scale of the amplitude is
arbitrary and the field is plotted as a function of angle for two
values of constant radius and as a function of radius for two values of
constant angle. The remarks which follow pertain as well to the field
amplitudes for other values of radius and angle which have not been
plotted although they are contained in the computer output.

Unfortunately, obtaining the field as a function of angle
is relatively time consuming since the time varies as the square of
the number of angular points and only linearly with the number of
radial points. This is the resul of gridding along lines of constant x
rather than r as described in section 4. The following figures there-
fore generally give only a sketchy indication of the angular variation
although the radial variation is given in some detail.

Since the wavelength is smaller for $\lambda = 100$ than for $\lambda = 10$
it is not surprising that the $\lambda = 100$ curves are more oscillatory.
The most striking feature of these plots is that the field is nearly
separable. For example the number of nodes in the radial function
is independent of the value of the angle. Separability generally
seems to be poorest in the vicinity of the source.

-22-

Figure 5-1

$\lambda = 10$

$r_2 = 19,880$ km

$x = +.2$

640 radial points

x 109.03 km

-23-
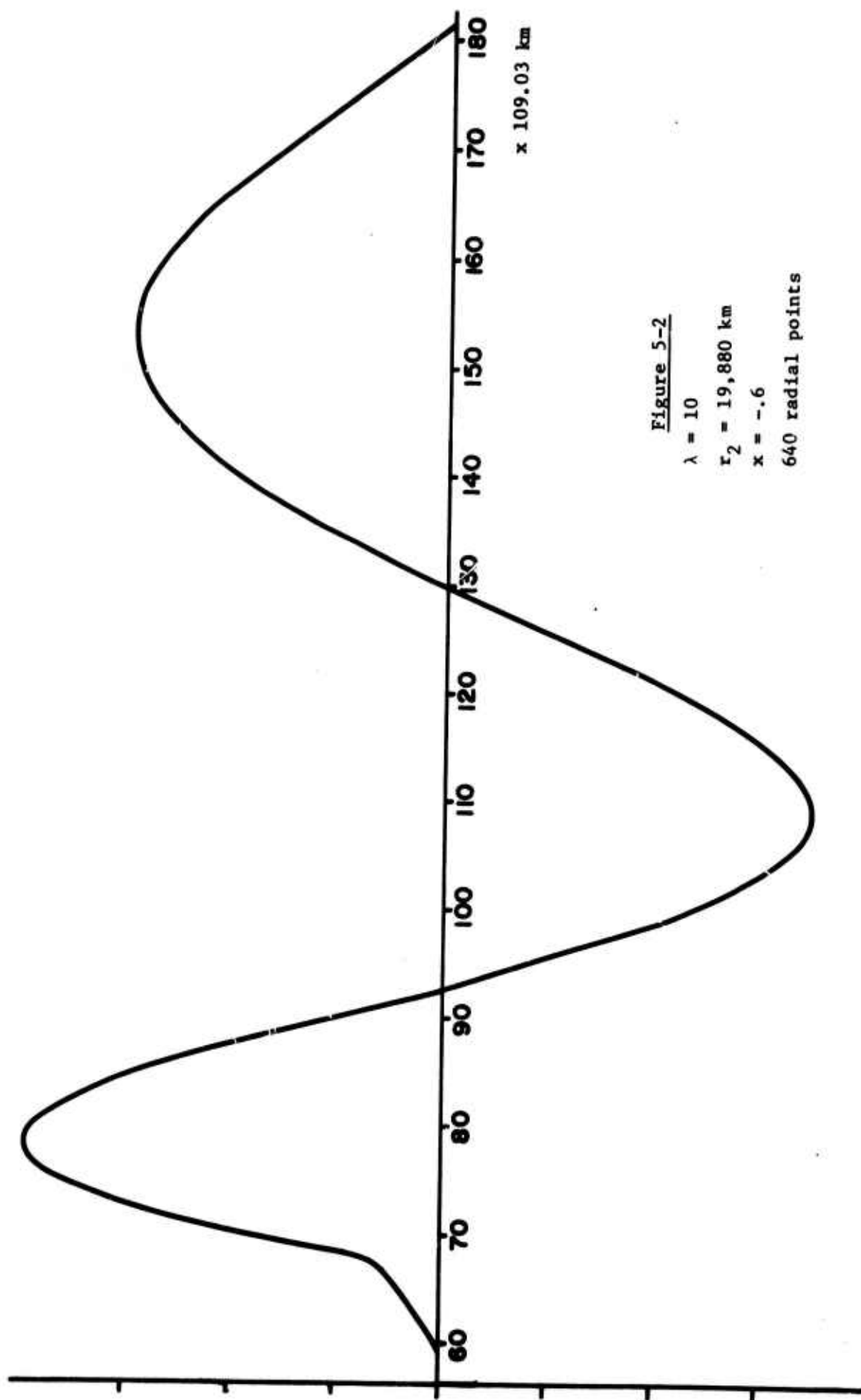
Figure 5-2

$\lambda = 10$

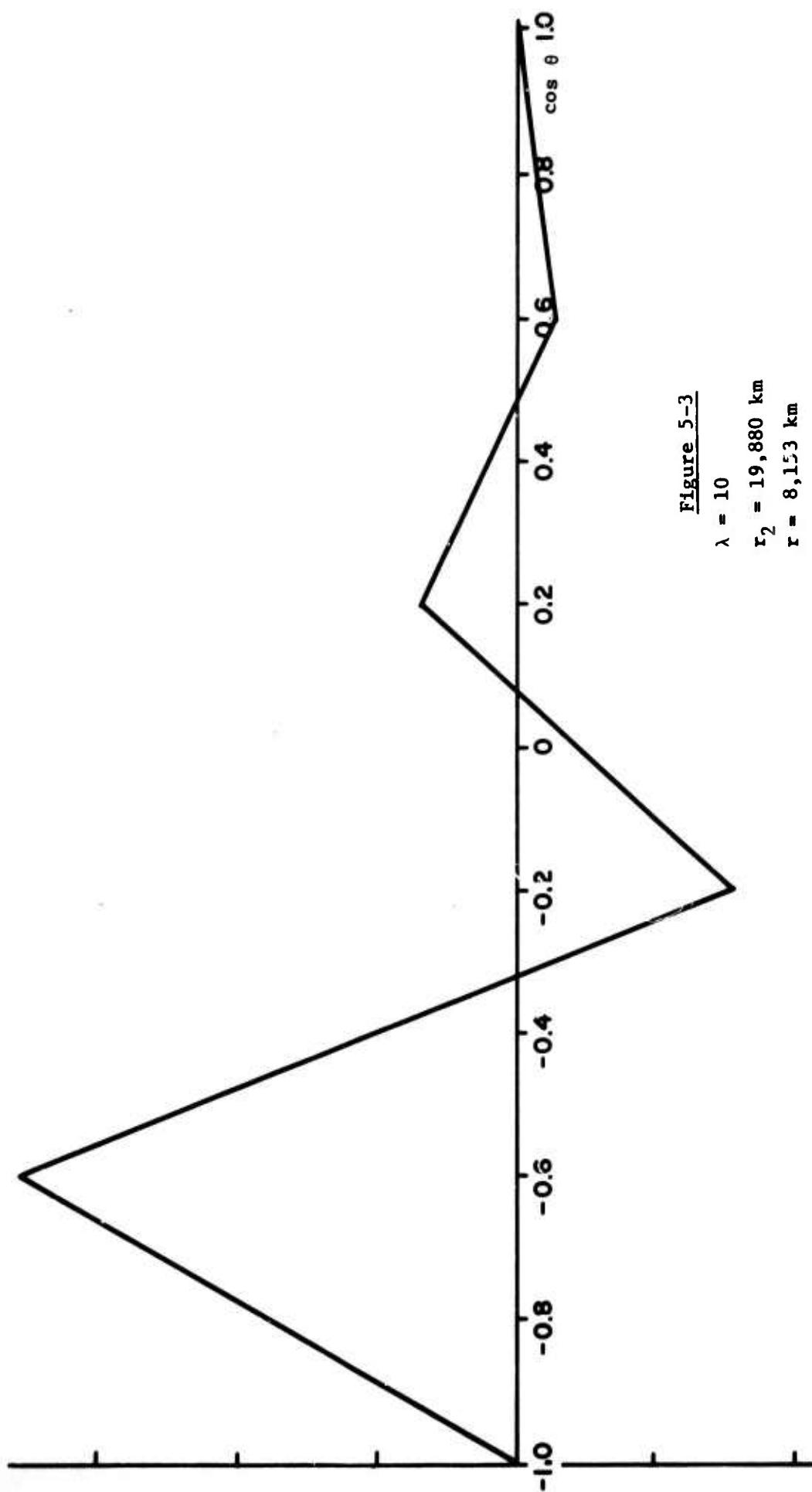$r_2 = 19{,}880$ km

$x = -.6$

640 radial points

x 109.03 km

-24-

Figure 5-3

$\lambda = 10$

$r_2 = 19{,}880$ km

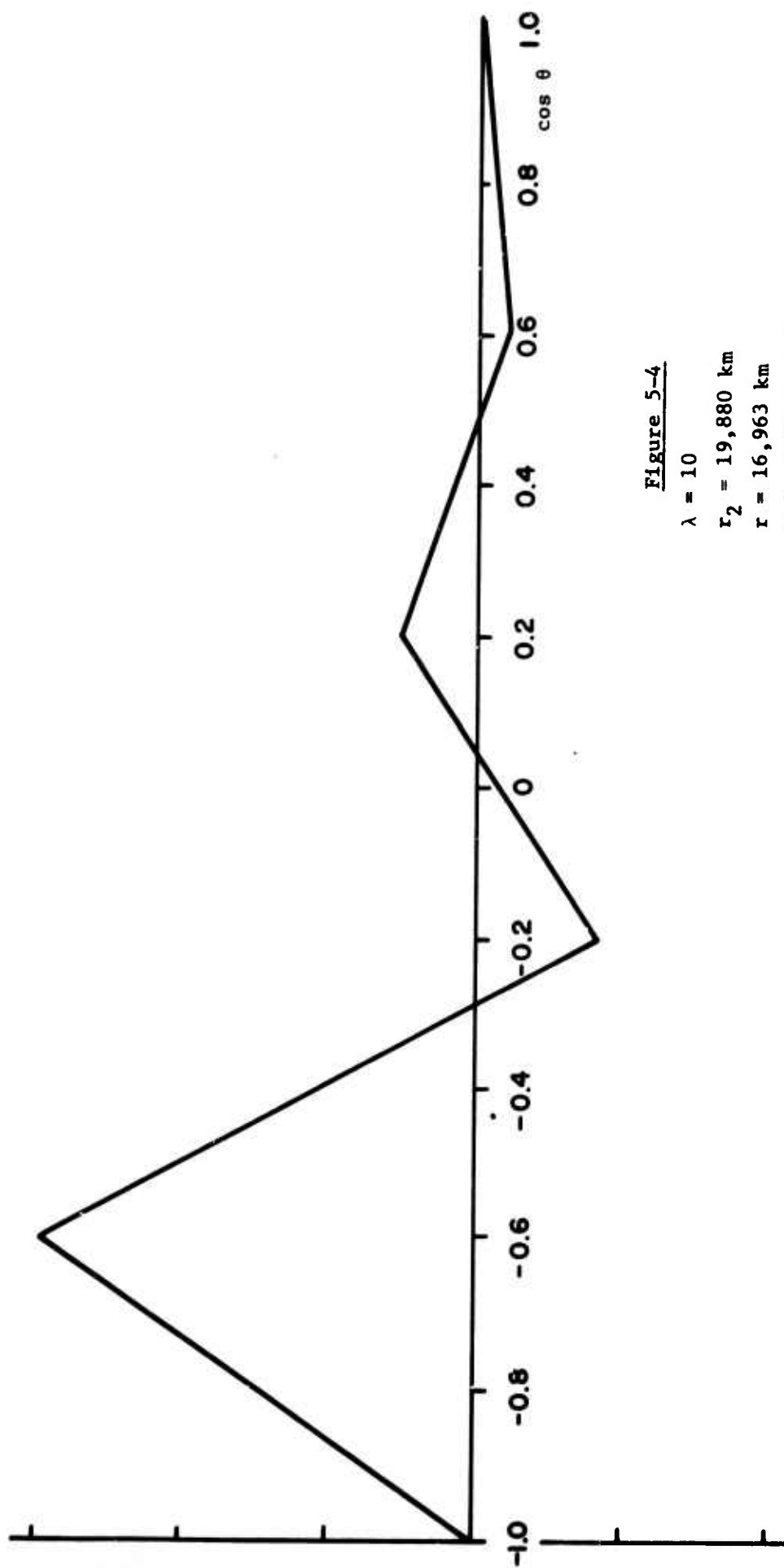$r = 8{,}153$ km

5 angular points

Figure 5-4

$\lambda = 10$

$r_2 = 19,880$ km

$r = 16,963$ km

5 angular points

cos θ
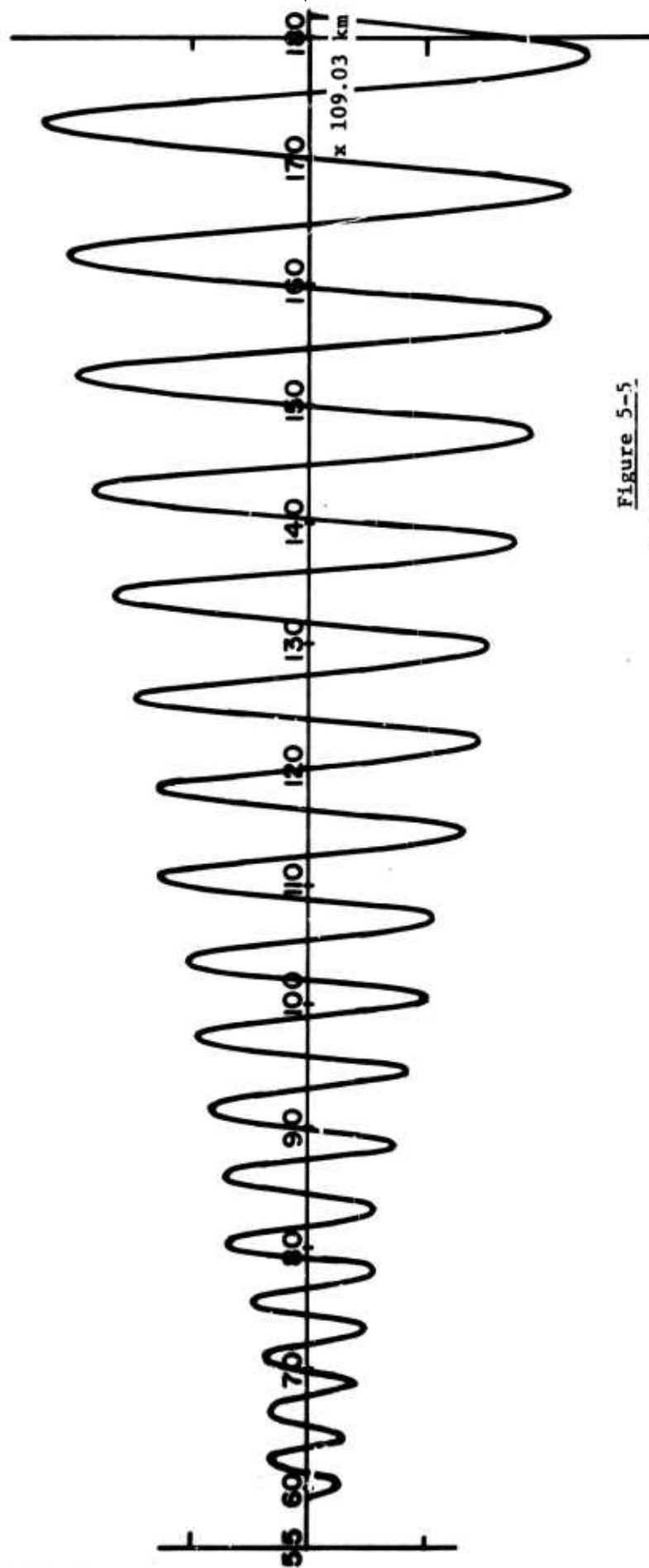
-26-

Figure 5-5

$\lambda = 100$
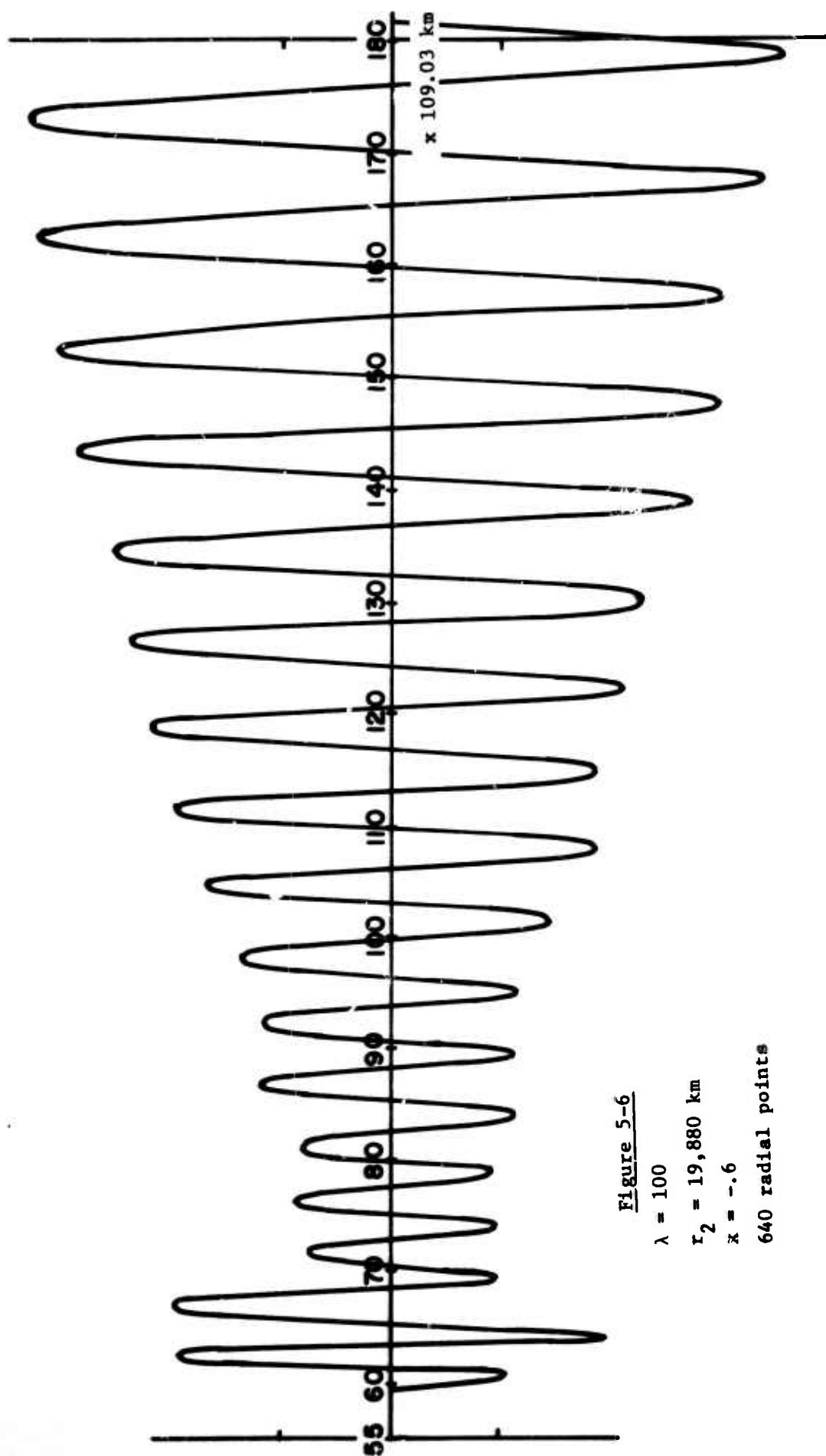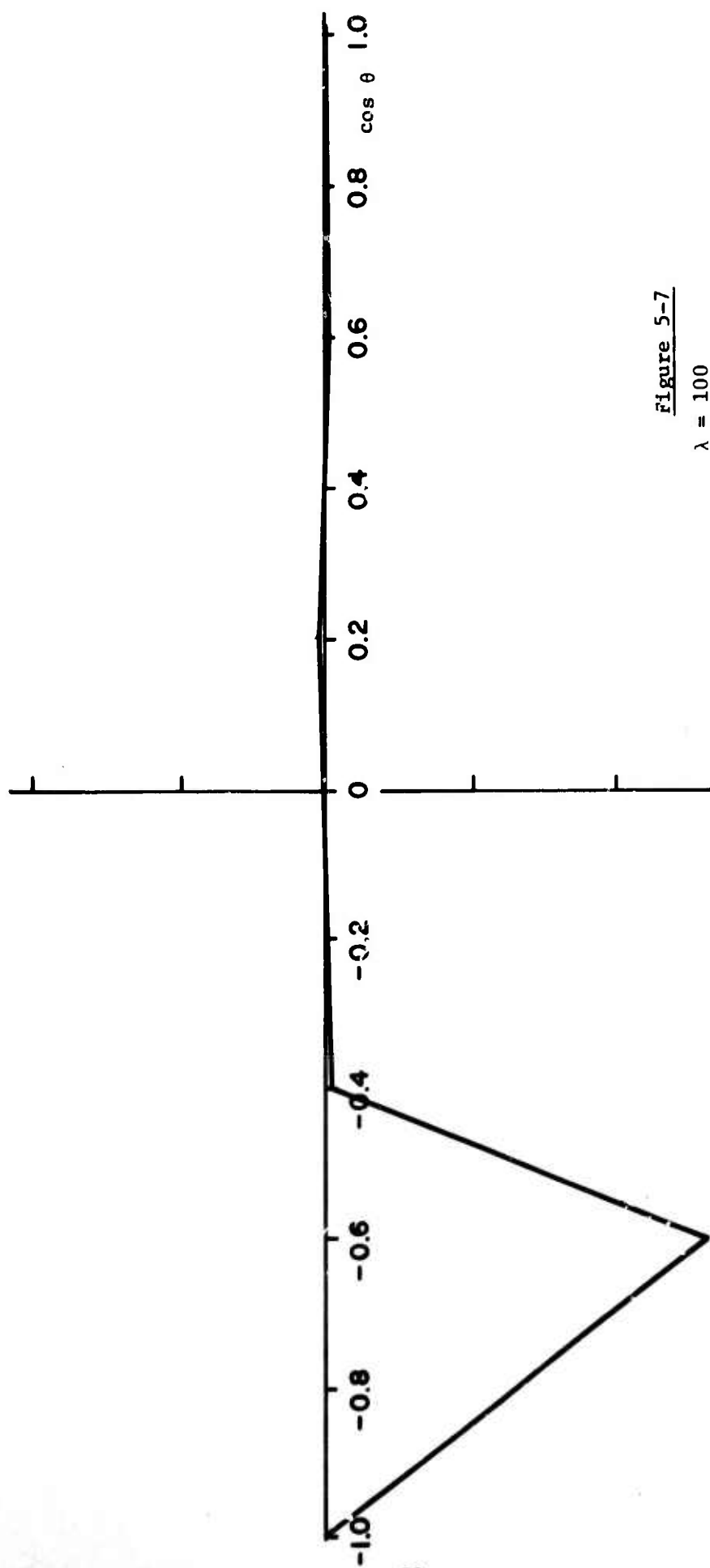
$r_2 = 19,880$ km

$x = +.2$

640 radial points

x 109.03 km

Figure 5-6

$\lambda = 100$

$r_2 = 19,880$ km

$x = -.6$

640 radial points

x 109.03 km

-28-

Figure 5-7

$\lambda = 100$

$r_2 = 19,880$ km

$r = 8,153$ km
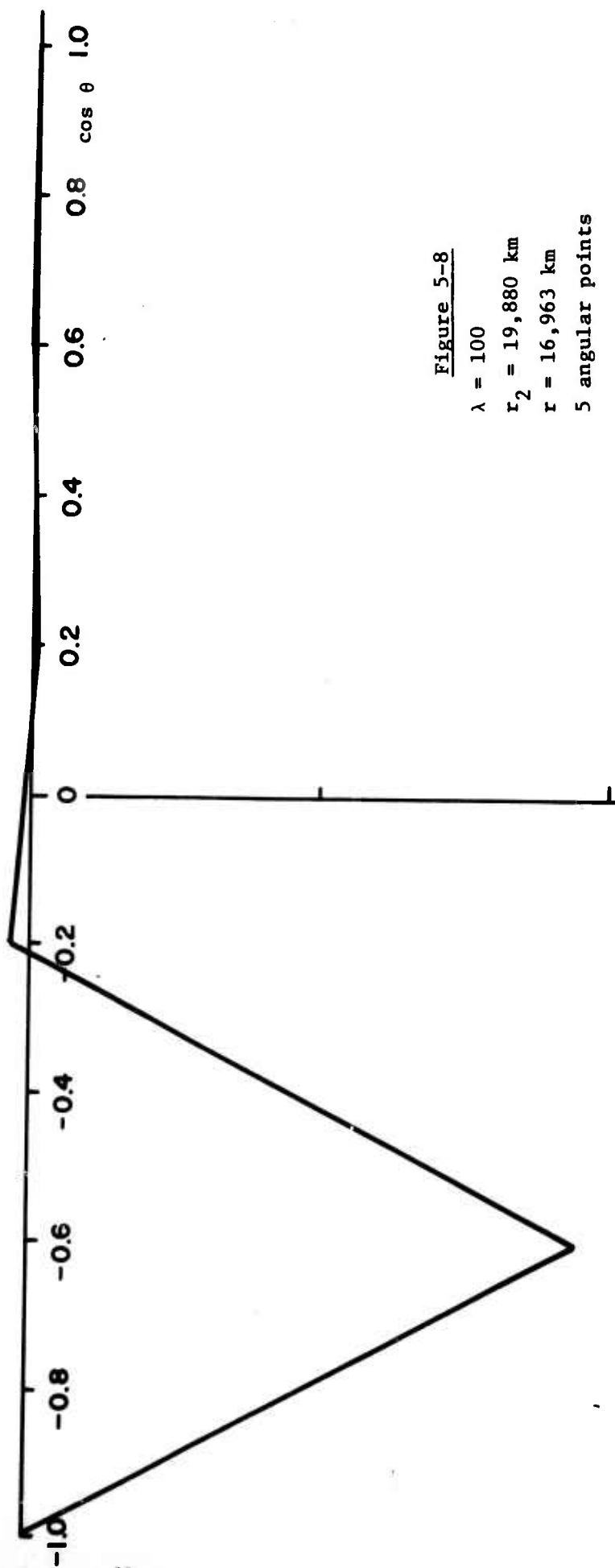
5 angular points

Figure 5-8

$\lambda = 100$

$r_2 = 19,880$ km

$r = 16,963$ km

5 angular points

This observation suggests that one term in the series (3-25) is dominant, and this is in fact the case. The dominant term is, roughly speaking, the one with the smallest value of $|\alpha_m|$ and its dominance apparently arises through the $\left(\alpha_m^2 - \frac{1}{4}\right)^{-1}$ factor occuring in each term of (3-25). The other terms seem to be of secondary importance because they are all of the same size but of random phase.

Obviously, this can only be true if we are not near an eigenfrequency, for then $\alpha_m \approx \ell + \frac{1}{2}$, where ℓ is an integer, and the dominance of one term occurs through the $\left(\cos \alpha_m \pi\right)^{-1}$ factor in each term of (3-25).

The actual dominant m value ($\bar{m}$) may be such that α_m is either the smallest real or the smallest imaginary value of α_m. We have at present no way of predicting which of these two possibilities will occur.

Figures (5-9) through (5-12) show two cases where $\alpha_{\bar{m}}$ is the smallest imaginary value of α_m.

In the first case $\lambda = 90$ and r_2 is again 19,880 km in the second case $\lambda = 59.5$ and r_2 is decreased to 8,370 km. The major difference between these figures and Figures (5-1) through (5-8) is that the angular function is now damped going away from the source. This makes sense because when α_m is imaginary the angular variation of the $\bar{m}$th term of (3-25) is the conical function $P'_{-1/2 + i|\alpha_m|}\left[\cos(\pi - \theta)\right]$ which is monotonic decreasing. A few of these functions are tabulated in our previous report[6] for small $|\alpha_m|$.

For $|\alpha_m|$ large the factor $\dfrac{P'_{-1/2 + i|\alpha_m|}(x_o)\, P'_{-1/2 + i|\alpha_m|}(-x)}{\cos |\alpha_m|\pi}$ which gives the angular variation of the $\bar{m}$th term is just proportional to $\dfrac{e^{-|\alpha_m|(\theta - \theta_o)}}{\sqrt{\sin \theta}}$. The fall off in Figure (5-12)
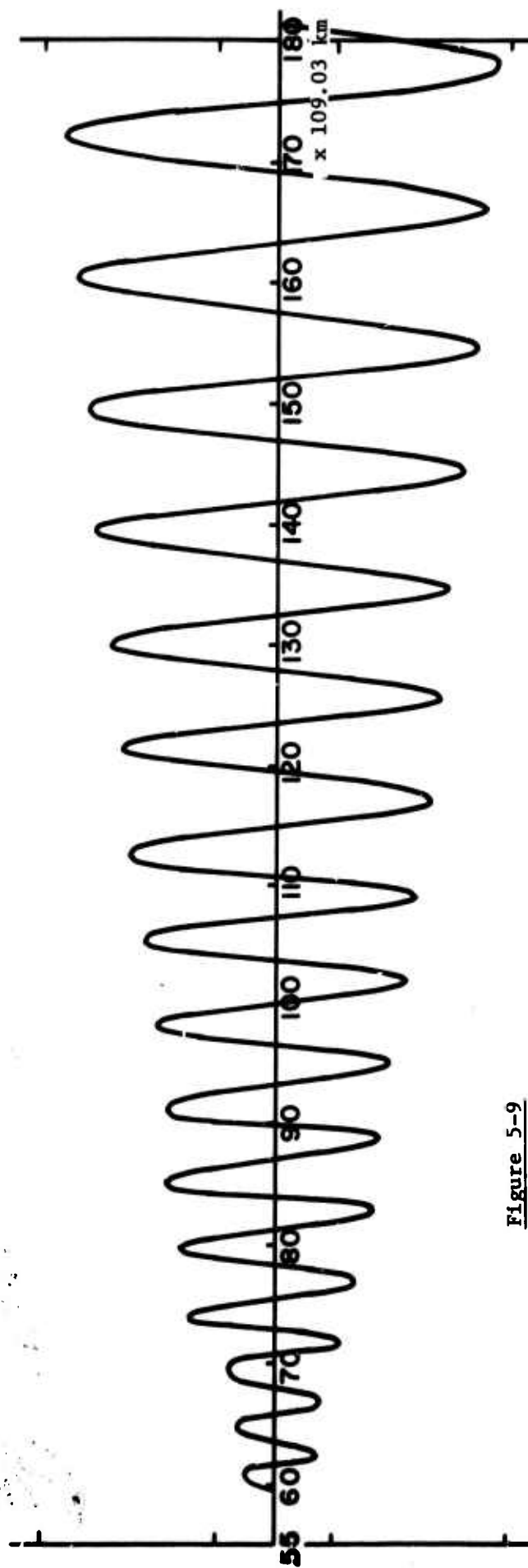
Figure 5-9

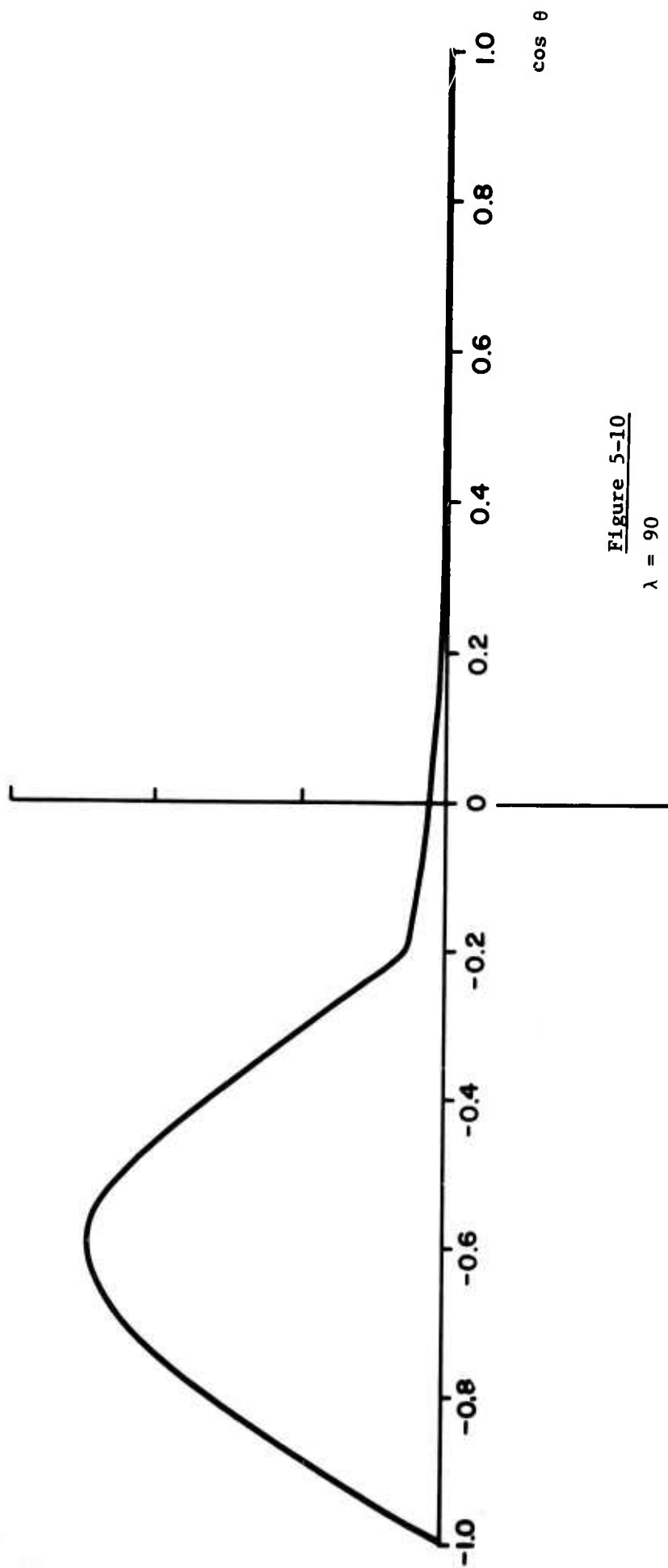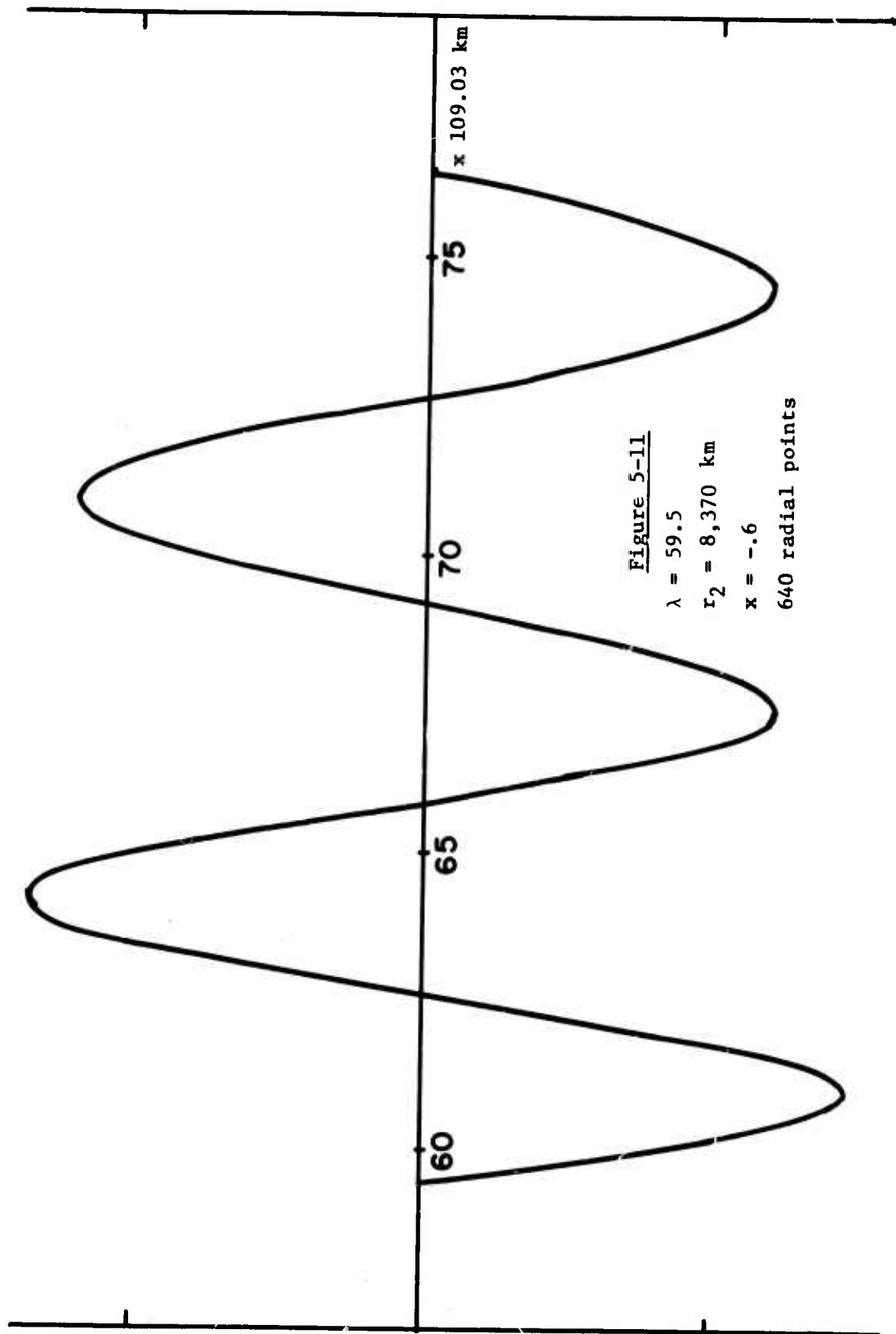$\lambda = 90$

$r_2 = 19,880$ km

$x = -.6$

640 radial points

Figure 5-10

$\lambda = 90$

$r_2 = 19,880$ km

$r = 8,153$ km

5 angular points

cos θ

-33-

Figure 5-11

$\lambda = 59.5$

$r_2 = 8,370$ km

$x = -.6$

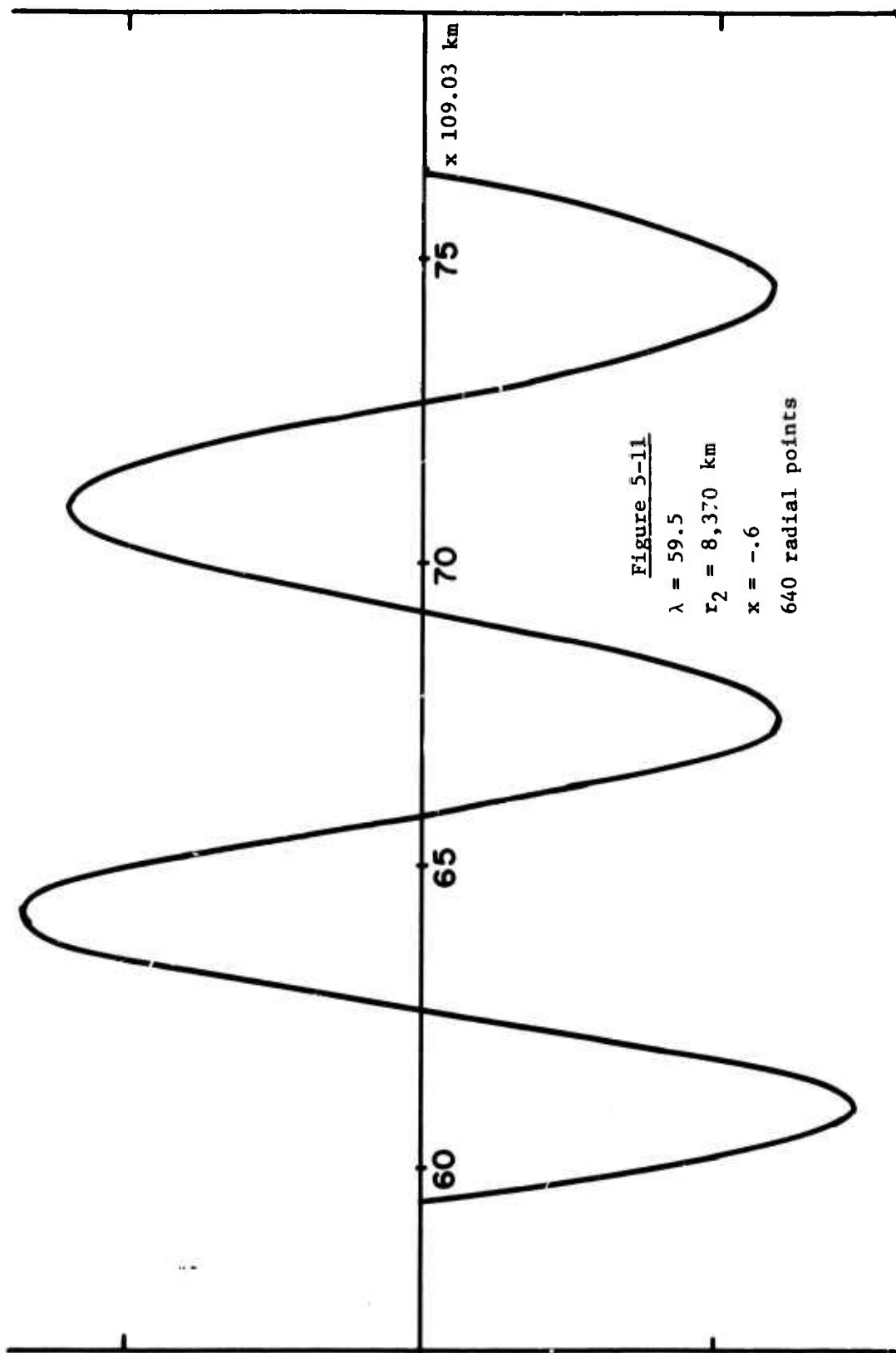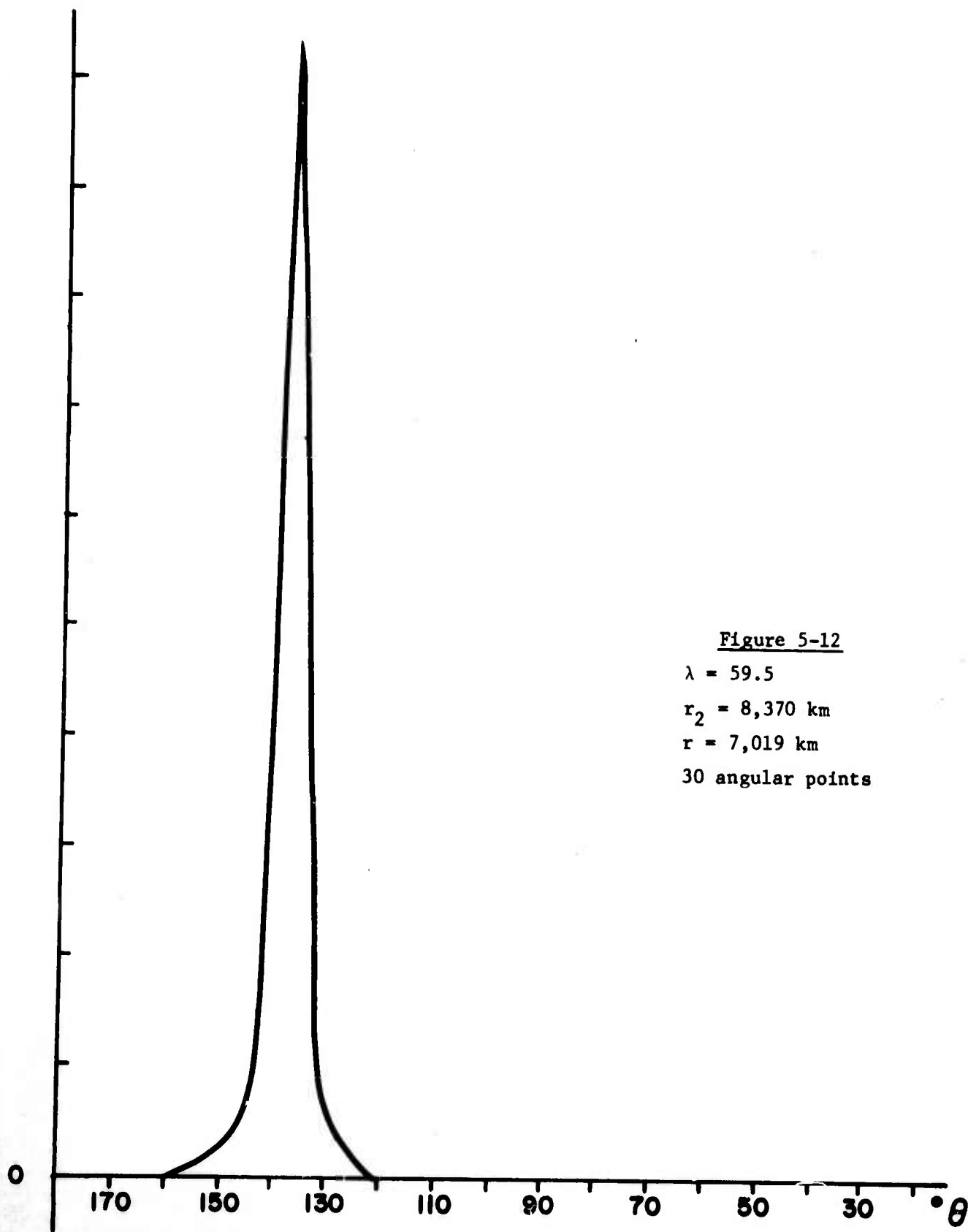640 radial points

x 109.03 km

60   65   70   75

Figure 5-11

$\lambda = 59.5$

$r_2 = 8,370$ km

$x = -.6$

640 radial points

x 109.03 km

Figure 5-12

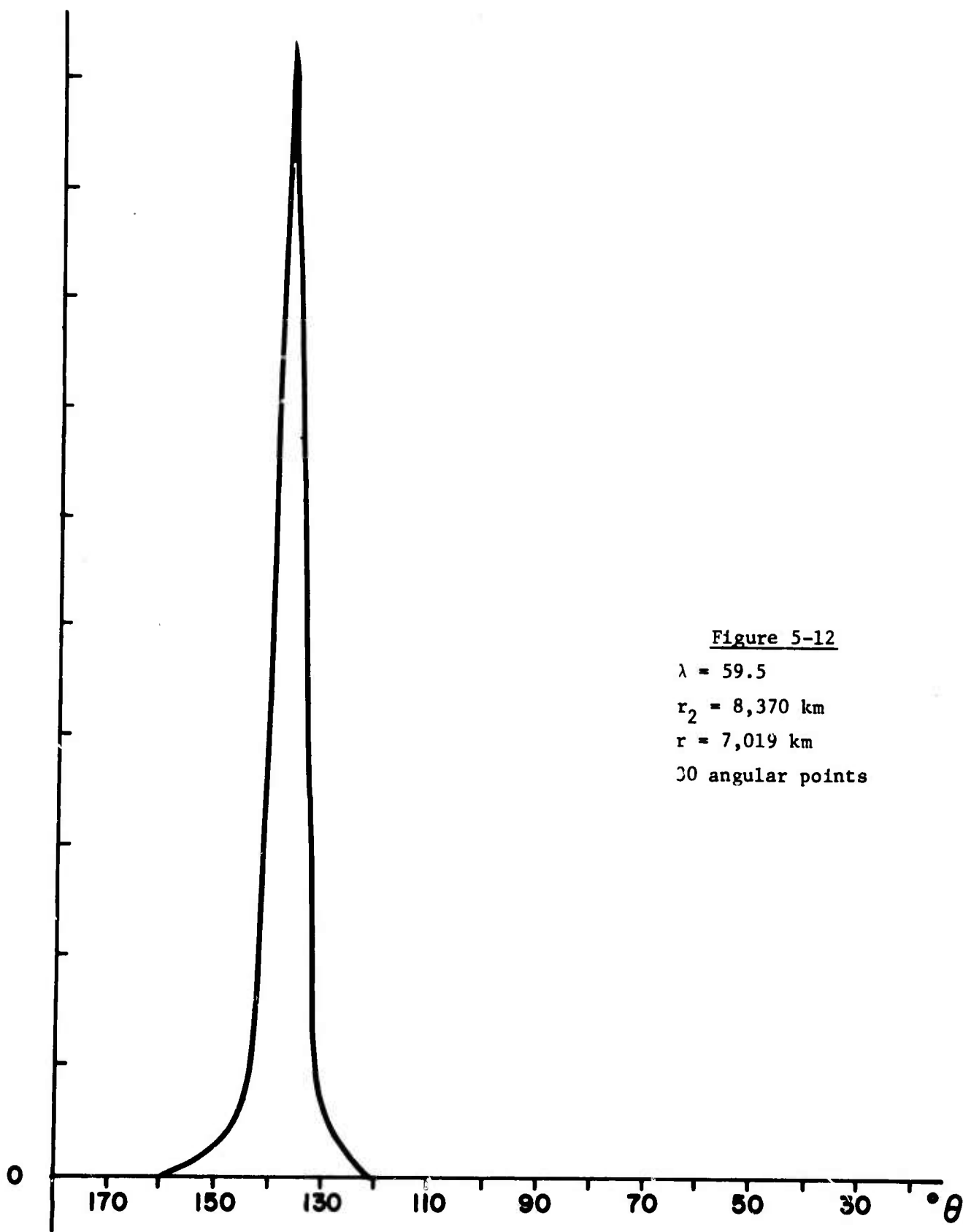$\lambda = 59.5$

$r_2 = 8,370$ km

$r = 7,019$ km

30 angular points

Figure 5-12

$\lambda = 59.5$

$r_2 = 8,370$ km

$r = 7,019$ km

30 angular points

should in theory be characterized by $|\alpha_{\overline{m}}| \gtrsim 20$; in fact, it is more like $|\alpha_{\overline{m}}| \gtrsim 10$. This discrepency, we think, arises from the difficulty the difference equations described in section 4 have in following the rapidly decreasing exponential function.

Table (5-13) illustrates the results of a number of runs with $r_2 = 19,880$ km and with various λ values.

The number of nodes in the radial function (second column) is determined from the computer output. $\alpha_{\overline{m}}$ is found from (3-31) and (3-32) with $\widetilde{m}$ equal the number of nodes listed in the preceding column plus one. In every case with constant λ investigated thus far $\alpha_{\overline{m}}$ has been either the smallest real value of or the smallest imaginary value.

In the last column, the number of nodes anticipated in the angular function is computed by assuming that when $\alpha_{\overline{m}}$ is real the angular function will behave like $P_\ell'(-x)$ where ℓ is the nearest integer to $-\frac{1}{2} + \alpha_{\overline{m}}$.

In only one case have we used enough angular points to adequately test this hypothesis. For this case in which 20 lines of constant x were used and the parameters were: $\lambda = 59.5$ $r_2 = 19,880$, we find $\alpha_{\overline{m}} = 6.5$ and $\ell = 6$. The angular function does, in fact, have 5 internal nodes, in agreement with our hypothesis.

If it is true that the $\overline{m}$th term alone of (3-25) is a reasonably good approximation to the field we have:

$$E \approx \frac{2\pi i \omega}{c^2} I \left(\ln \frac{r_3}{r_1}\right)^{-1} (r_0 r)^{-\frac{1}{2}} \frac{P'_{-\frac{1}{2}+\alpha_{\overline{m}}}(x_0) P'_{-\frac{1}{2}+\alpha_{\overline{m}}}(-x)}{\cos \alpha_{\overline{m}}\pi \left(\alpha_{\overline{m}}^2 - \frac{1}{4}\right)} \tag{5-1}$$

$$\sin\left(\frac{\overline{m}\,\pi\,\ln\frac{r_2}{r_1}}{\ln\frac{r_2}{r_1}}\right) \sin\left(\frac{\overline{m}\,\pi\,\ln\frac{r}{r_1}}{\ln\frac{r_2}{r_1}}\right)$$

-36-

TABLE (5-13) $r_2 = 19,880$ km

λ	Number of Nodes of the Radial Function Excluding the End Points	$\alpha_{\overline{m}}$ is the smallest value of α_m	Number of Nodes of the Angular Function Excluding the End Points
10	2	real	4
20	6	real	10
30	10	imaginary	damped
40	13	real	5
50	16	real	16
59.5	20	real	5
60	20	real	9
70	24	imaginary	damped
80	26	real	23
90	31	imaginary	damped
100	34	real	15

The addition of finite conductivity according to (3-30) just adds a damping factor:

$$e^{-\frac{\omega}{8\pi\sigma}\frac{c^2}{V_A^2}|\alpha_{\bar{m}}|}$$

(5-2)

to (5-1) if σ is not too small and if $\alpha_m^r >> \alpha_m^i$.

We turn now to the case which introduces the angular variation characteristic of the dipole field: $\lambda = \dfrac{\lambda_o}{1+3x^2}$,

where λ_o is constant.

The results are shown in Figures (5-14) through (5-20) for $\lambda_o = 59.5$ and $r_2 = 19,880$. The primary effect of the $(1+3x^2)^{-1}$ factor is to increase the effective wavelength when $x \neq 0$. Of course, the separability evident in the solutions in the absence of this factor disappears.

One might expect that on each line of constant x that the radial dependence of a single term of (3-25) might still be picked out. This is the case but the value of $\bar{m}$ is no longer such that $\alpha_{\bar{m}}$, on that particular line, is a minimum. For example, at $x = -.6$ we expect $\bar{m} = 15$ ($\alpha_{\bar{m}}$ real) or $\bar{m} = 16$ ($\alpha_{\bar{m}}$ imaginary) but find instead $\bar{m} = 14$(13 internal nodes). The situation is best demonstrated at $x = 0$ where if the concept of the effective value of $\dfrac{\lambda_o}{1+3x^2}$ on a line of constant x were valid we would expect the two curves of Figure (5-16) to coincide. In actuality, the $1+3x^2$ curve has $\bar{m} = 13$ while the constant λ curve has $\bar{m} = 12$.

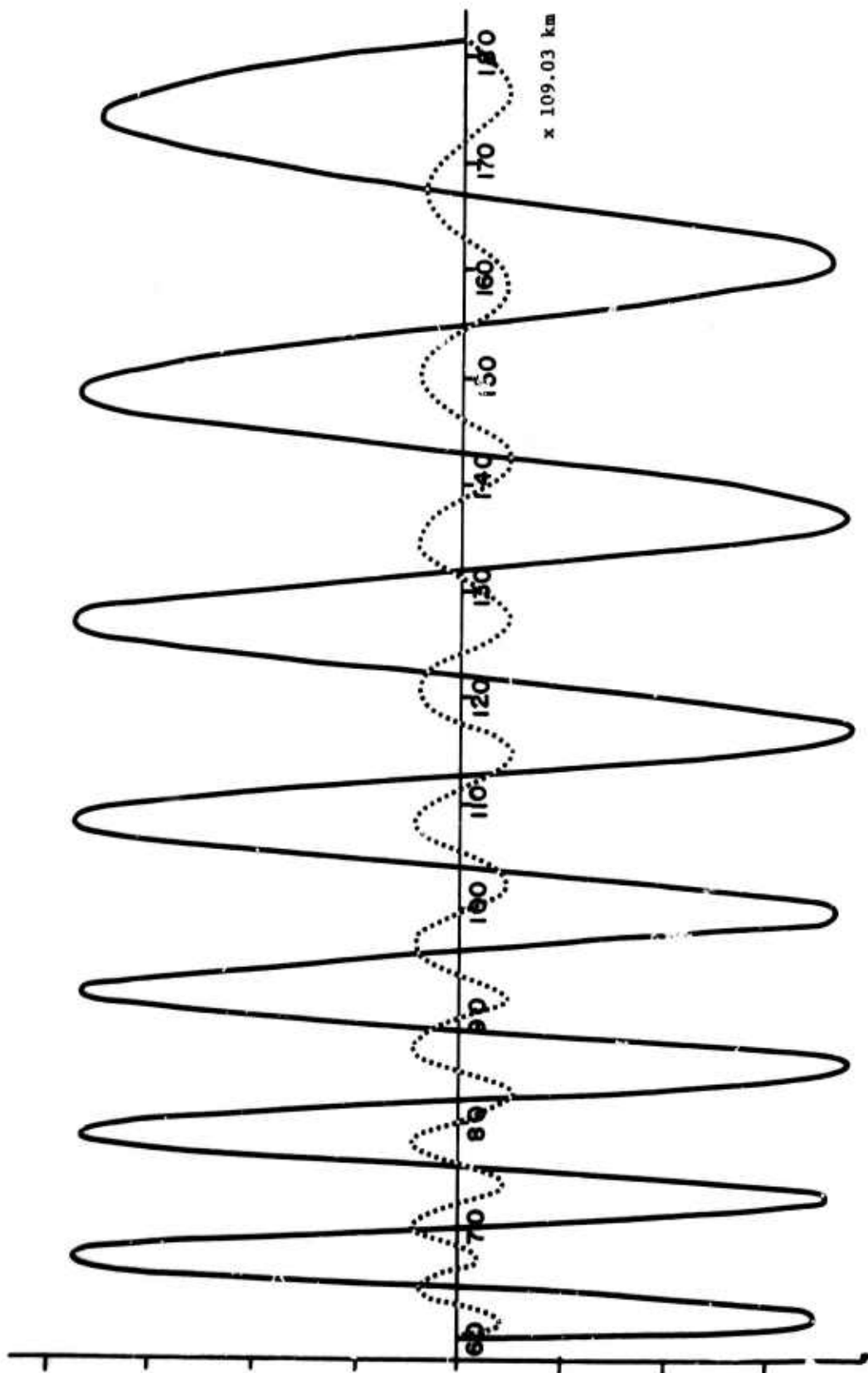Finally, we consider the case $\lambda = \dfrac{\lambda_o}{1+3x^2}$, where λ_o is a

Figure 5-14

$\lambda_o = 59.5$
$r_2 = 19,880$ km
$x = -.6$
640 radial points

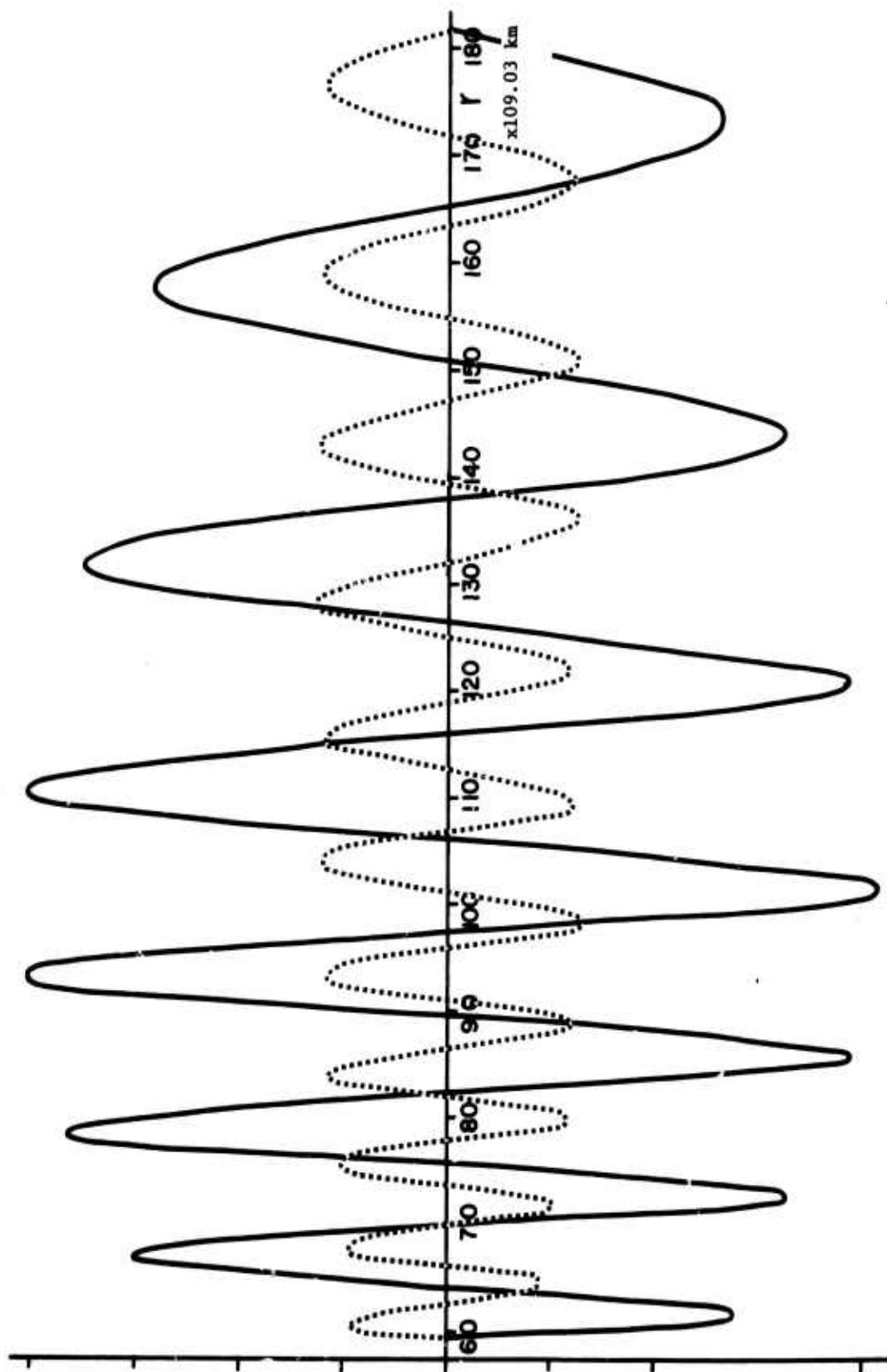$$\lambda = \frac{\lambda_o}{1 + 3x^2}$$

...... $\lambda = \lambda_o$

x 109.03 km

-39-

Figure 5-15

$$\lambda = \frac{\lambda_o}{1 + 3x^2}$$

...... $\lambda = \lambda_o$

$\lambda_o = 59.5$

$r_2 = 19,880$ km

$x = -.8$

640 radial points

x109.03 r km
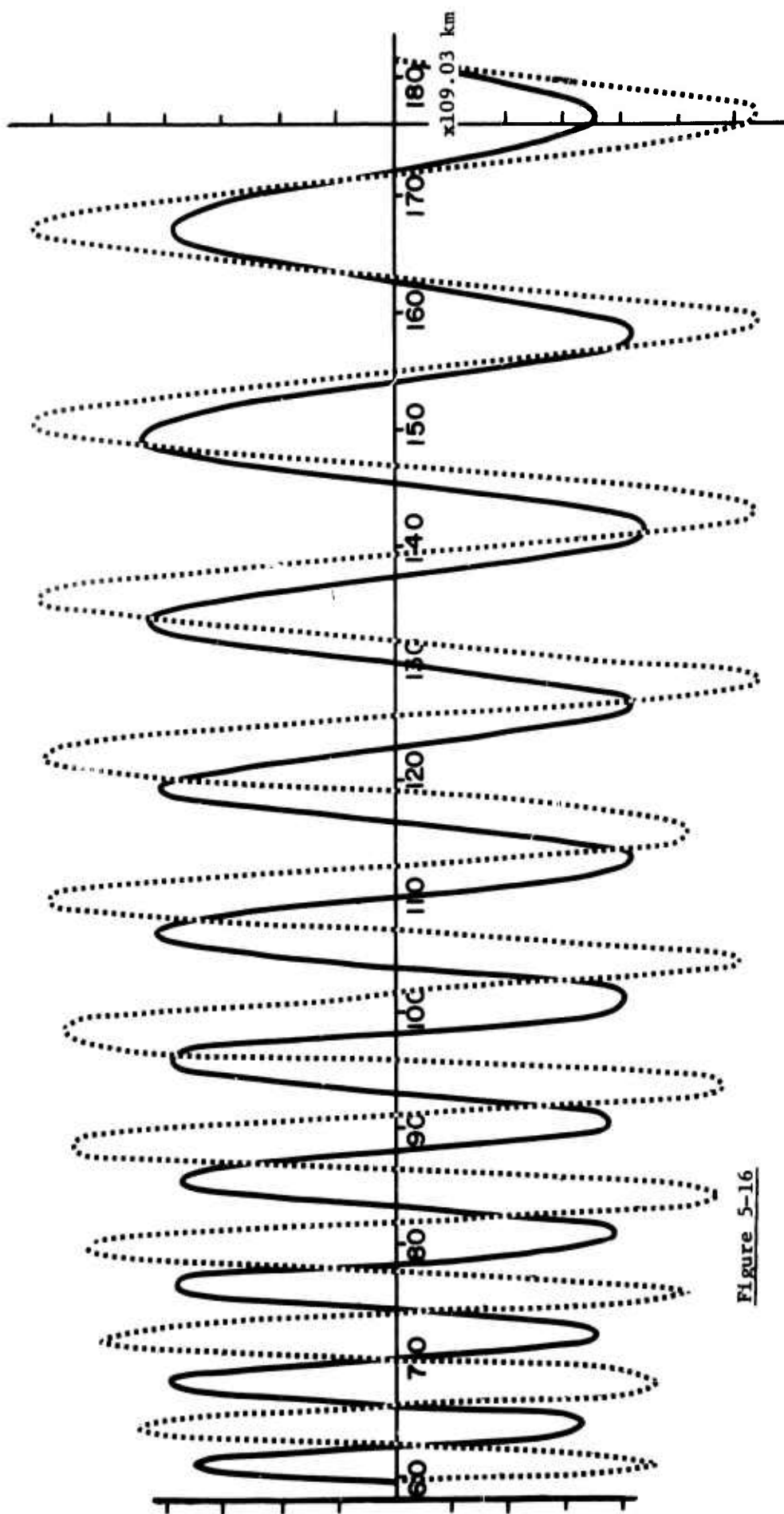
Figure 5-16

$\lambda_o = 59.5$ $r_2 = 19,880$ km

——— $\lambda = \dfrac{\lambda_o}{1 + 3x^2}$ $x = 0$

640 radial points

.... $\lambda = \lambda_o$
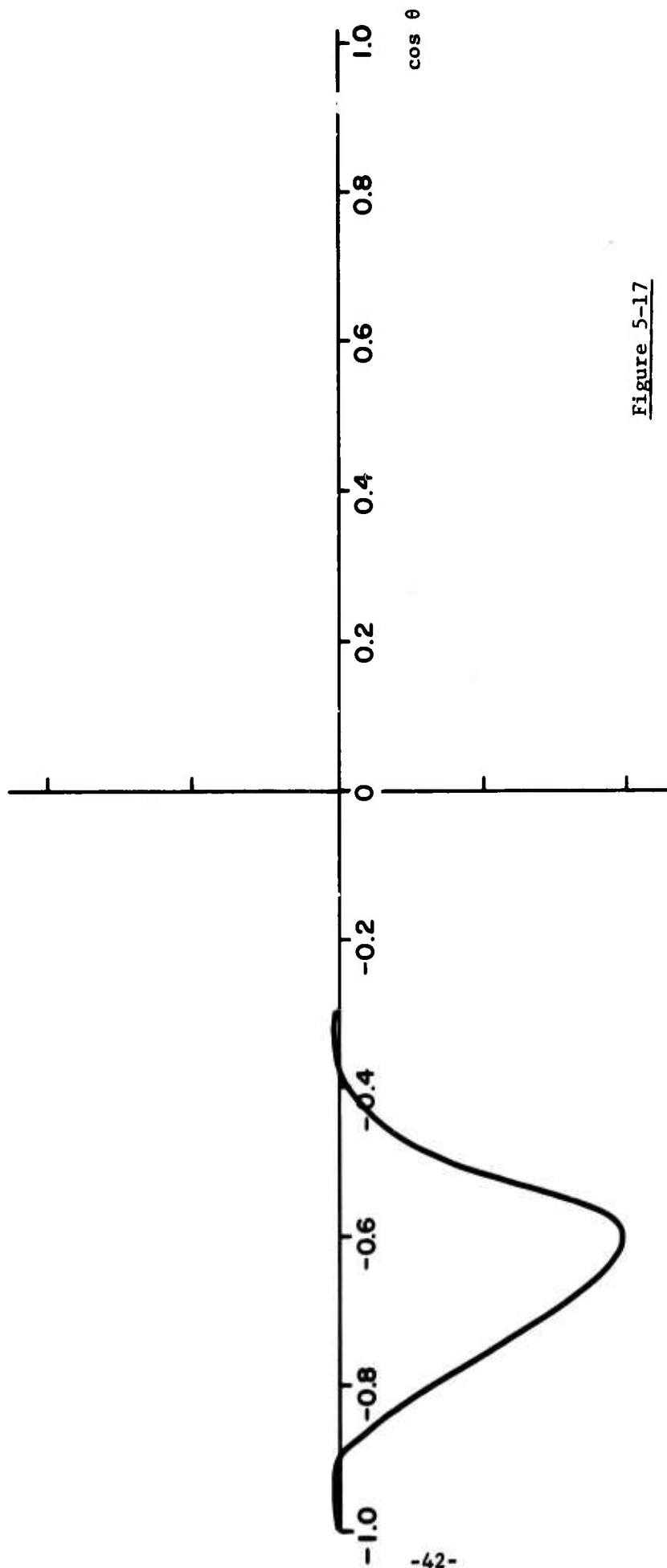
Figure 5-17

$$\lambda = \frac{\lambda_o}{1 + 3x^2}$$

$\lambda_o = 59.5$
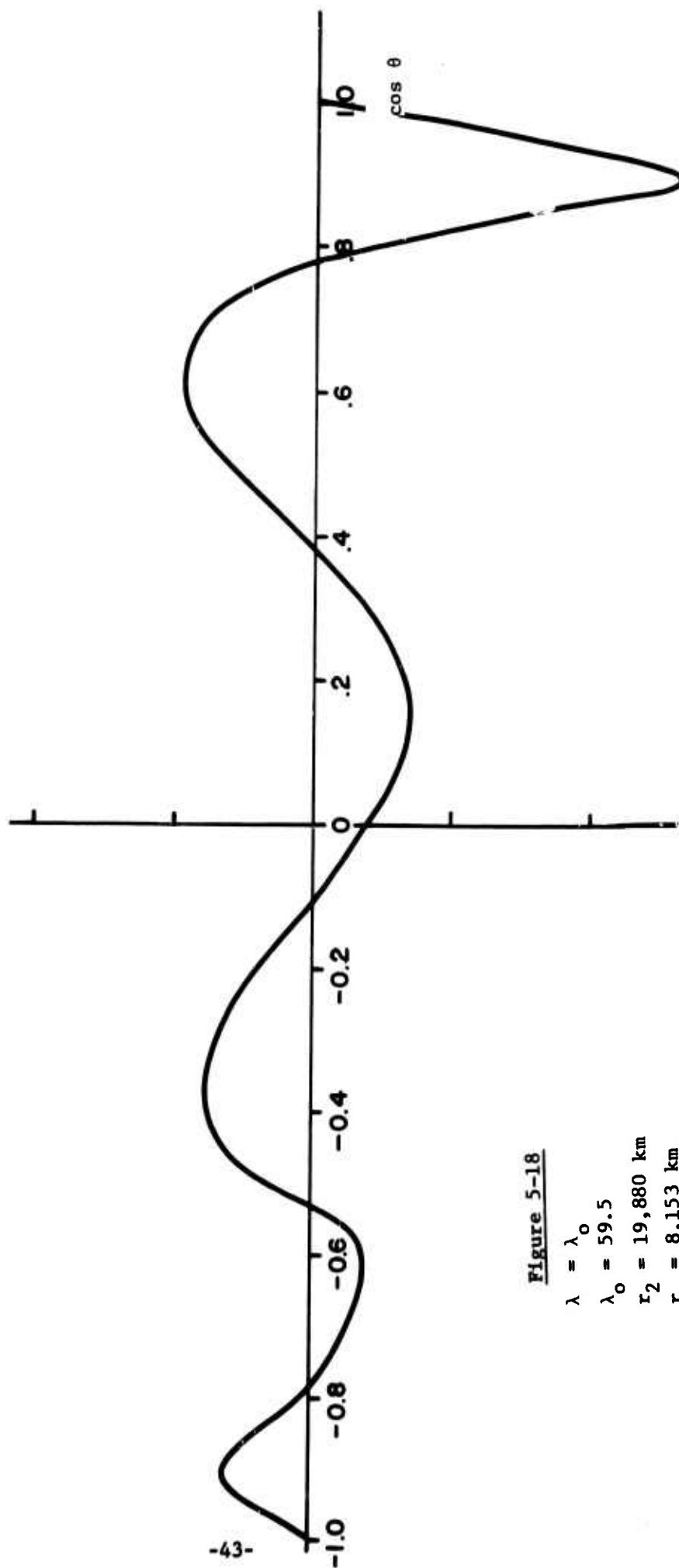
$r_2 = 19,880$ km

$r = 8,153$ km

20 angular points

cos θ

Figure 5-18

$\lambda = \lambda_0$

$\lambda_0 = 59.5$
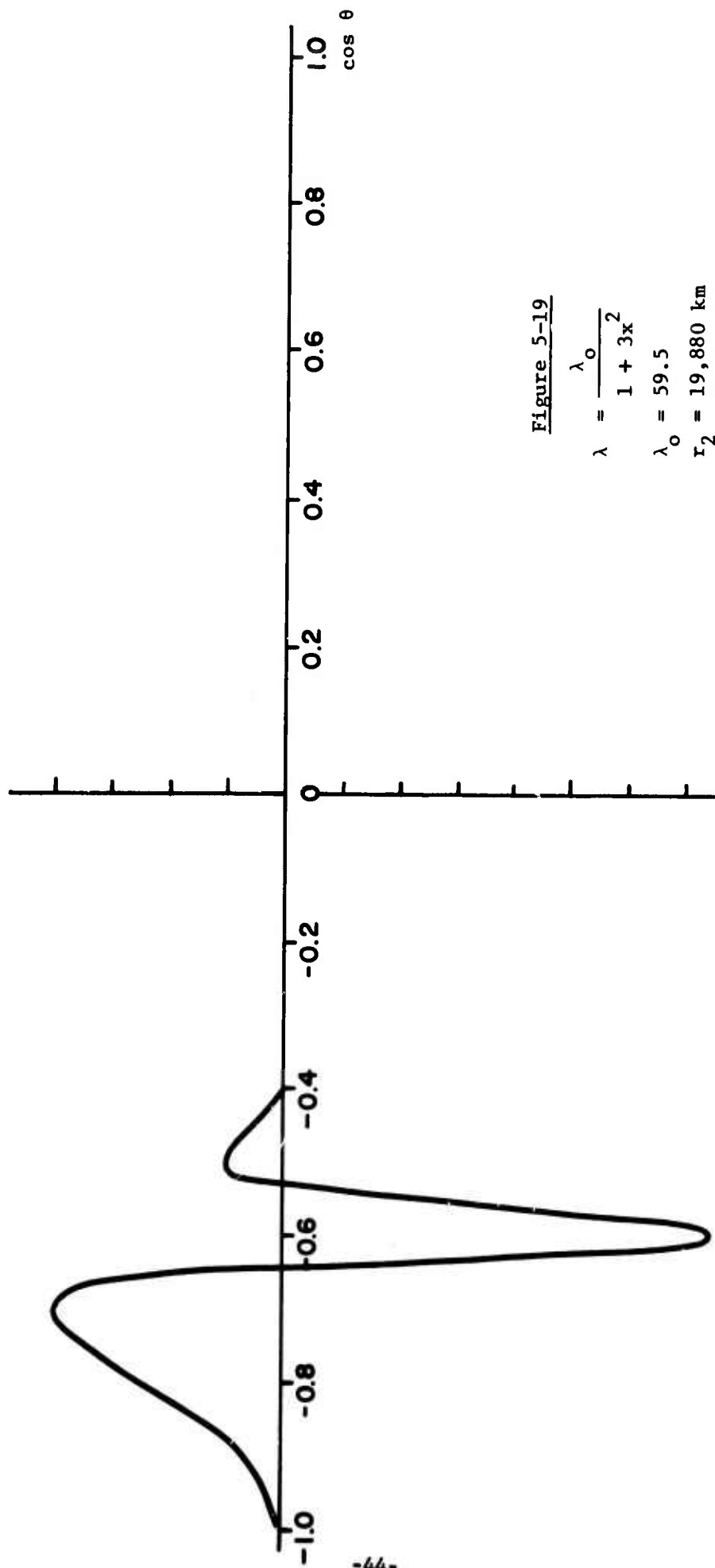
$r_2 = 19,880$ km

$r = 8,153$ km

20 angular points

-43-

cos θ

-44-

Figure 5-19

$$\lambda = \frac{\lambda_o}{1 + 3x^2}$$

$\lambda_o = 59.5$
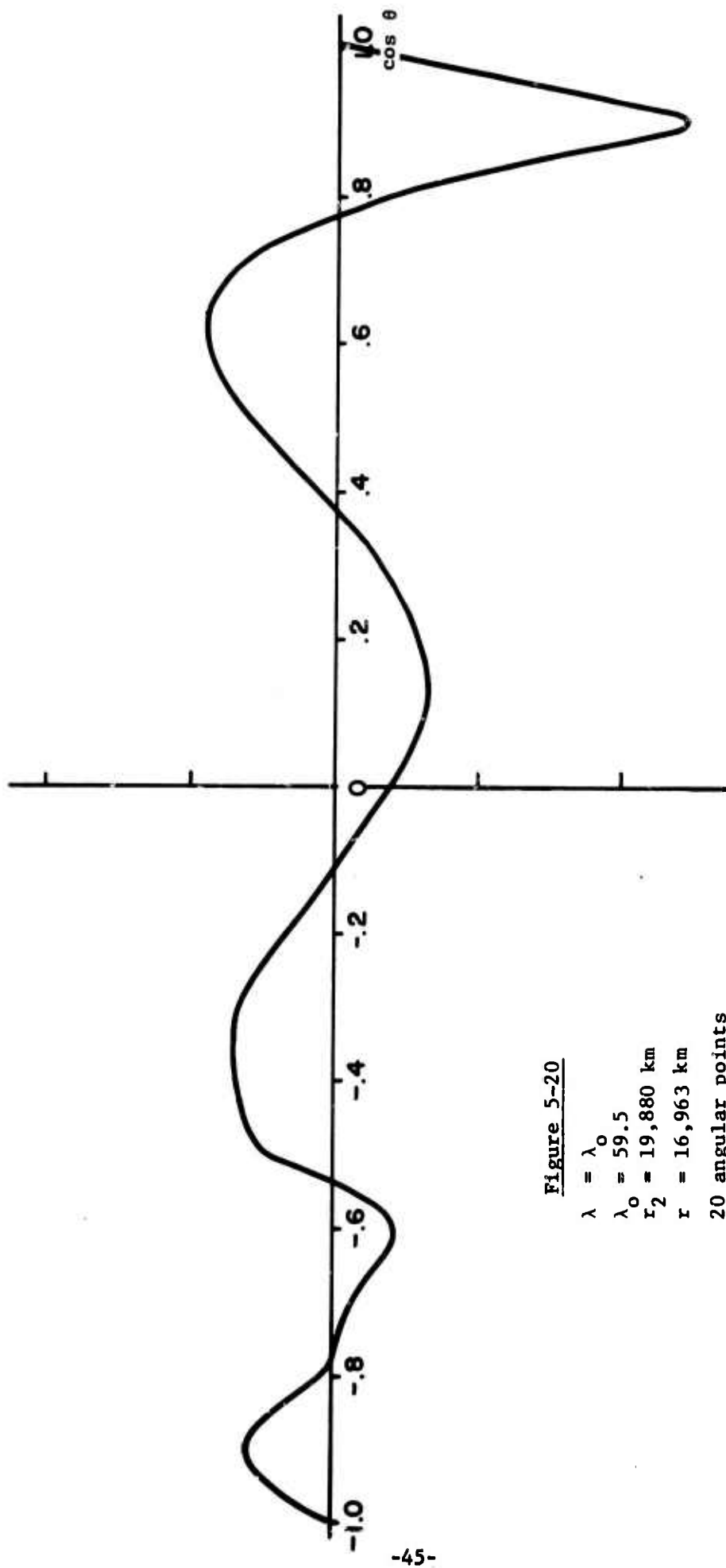
$r_2 = 19{,}880$ km

$r = 16{,}963$ km

20 angular points

1.0 0.8 0.6 0.4 0.2 0 -0.2 -0.4 -0.6 -0.8 -1.0

Figure 5-20

$\lambda = \lambda_o$
$\lambda_o = 59.5$
$r_2 = 19,880$ km
$r = 16,963$ km
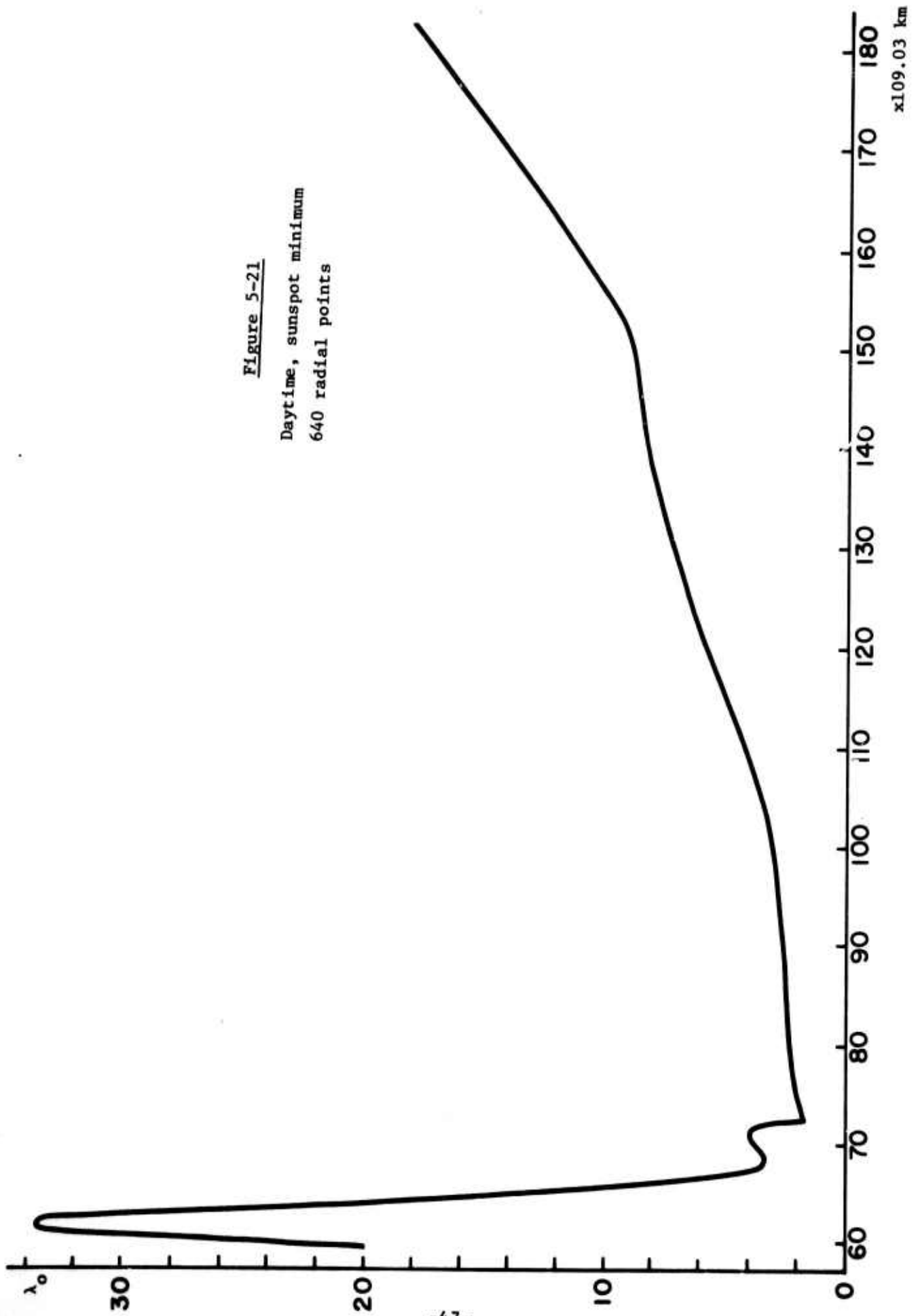20 angular points

-45-

function of r. λ_o is computed on the basis of the model ionosphere of Prince and Bostick[10] with $\omega = 1$ cps.

Figures (5-21) and (5-22) show λ_o for daytime and nighttime sunspot minimum, respectively.

Figures (5-23) and (5-24) show the radial and angular functions for a small cavity, $r_2 = 8,370$ km. λ_o is plotted next to the radial function and it is clear, for this particular case, that the radial function is insensitive to the detailed structure of λ_o.

Figures (5-25) and (5-26) show the radial and angular functions for a large cavity, $r_2 = 19,880$ km for the nighttime case. Figures (5-27) and (5-28) show the analogous daytime case. λ_o is larger in the daytime and hence the wavelength is smaller. This produces an additional node in the radial function in the daytime case.

Figure 5-21

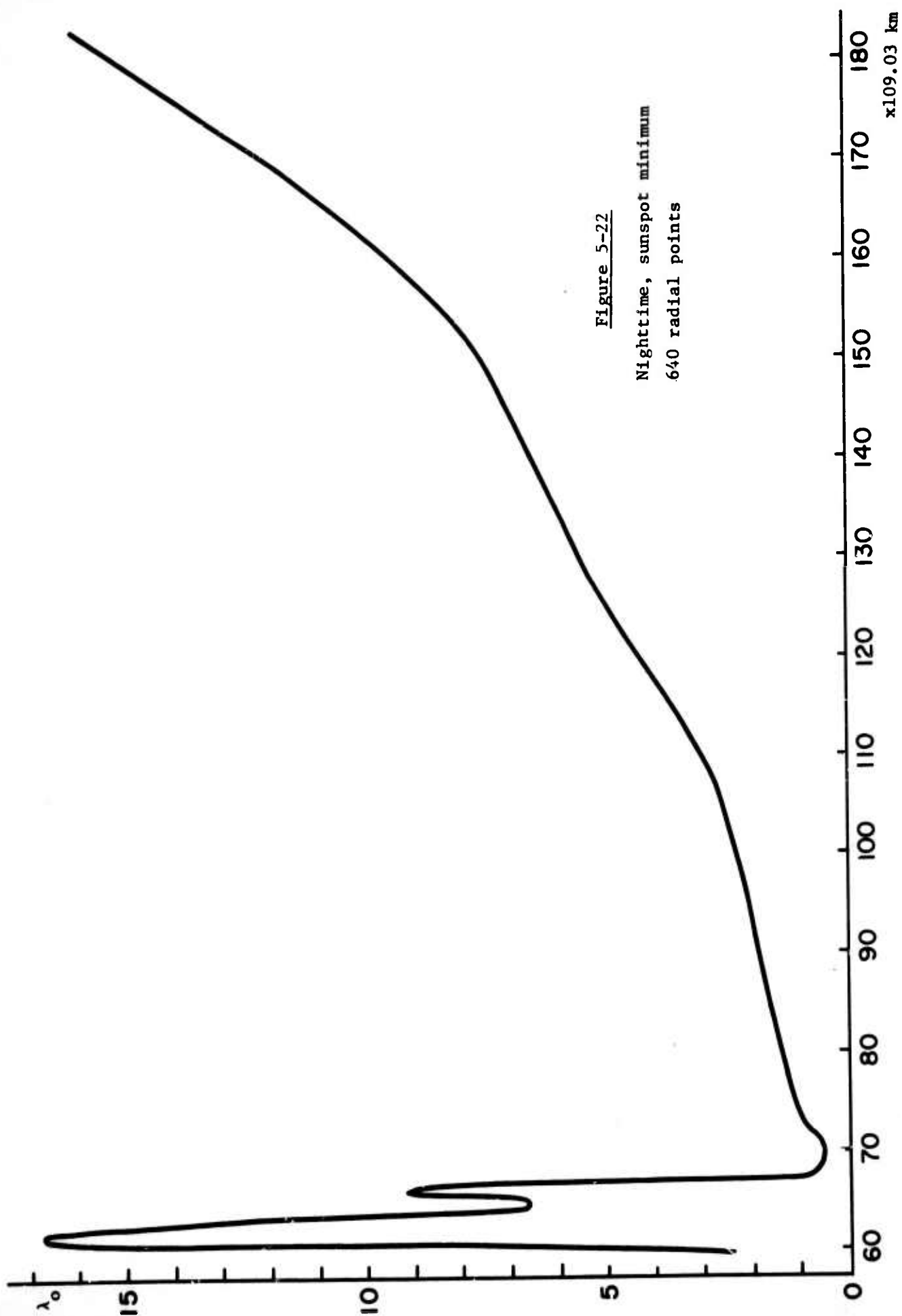Daytime, sunspot minimum

640 radial points

x109.03 km

Figure 5-22

Nighttime, sunspot minimum
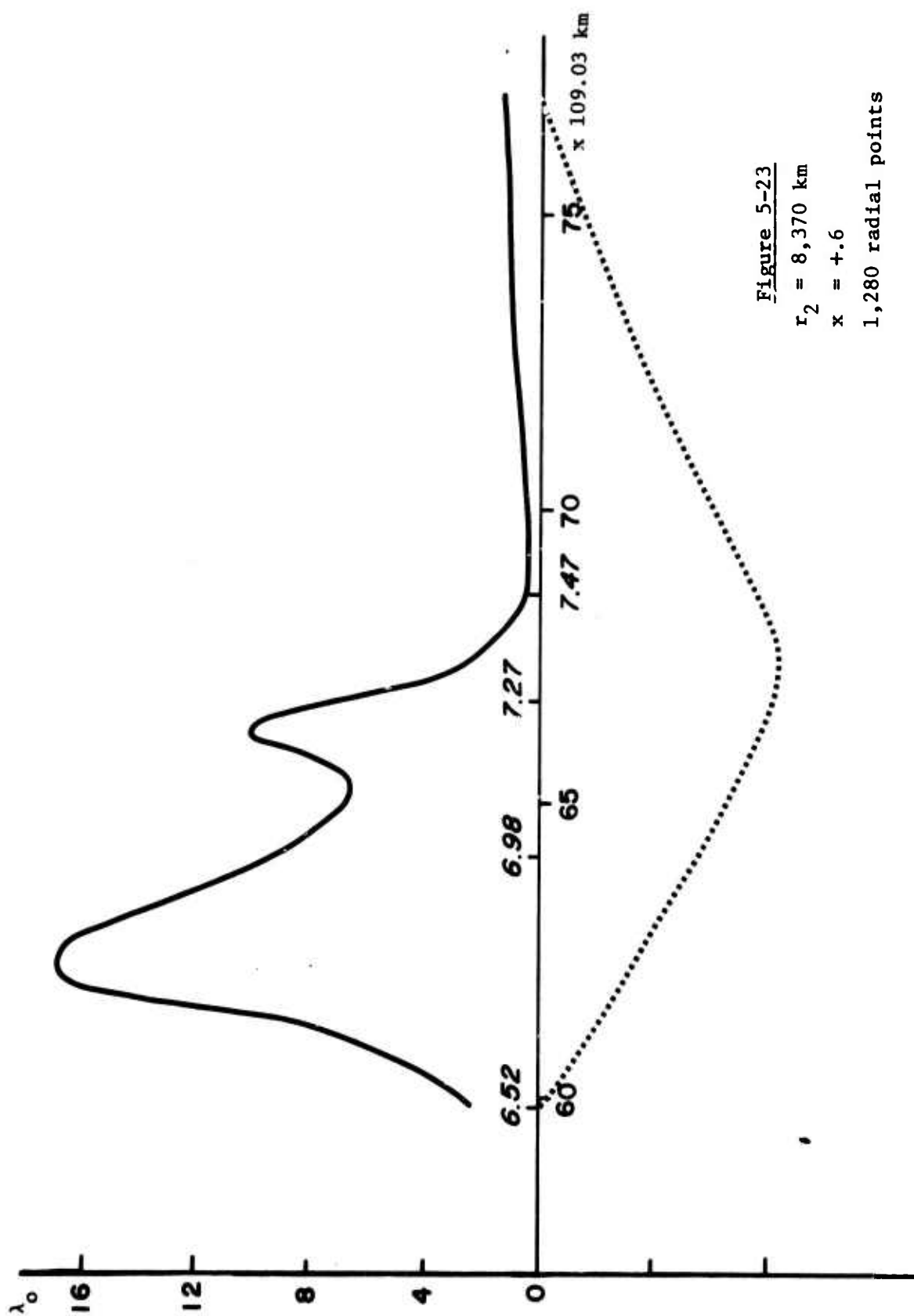
640 radial points

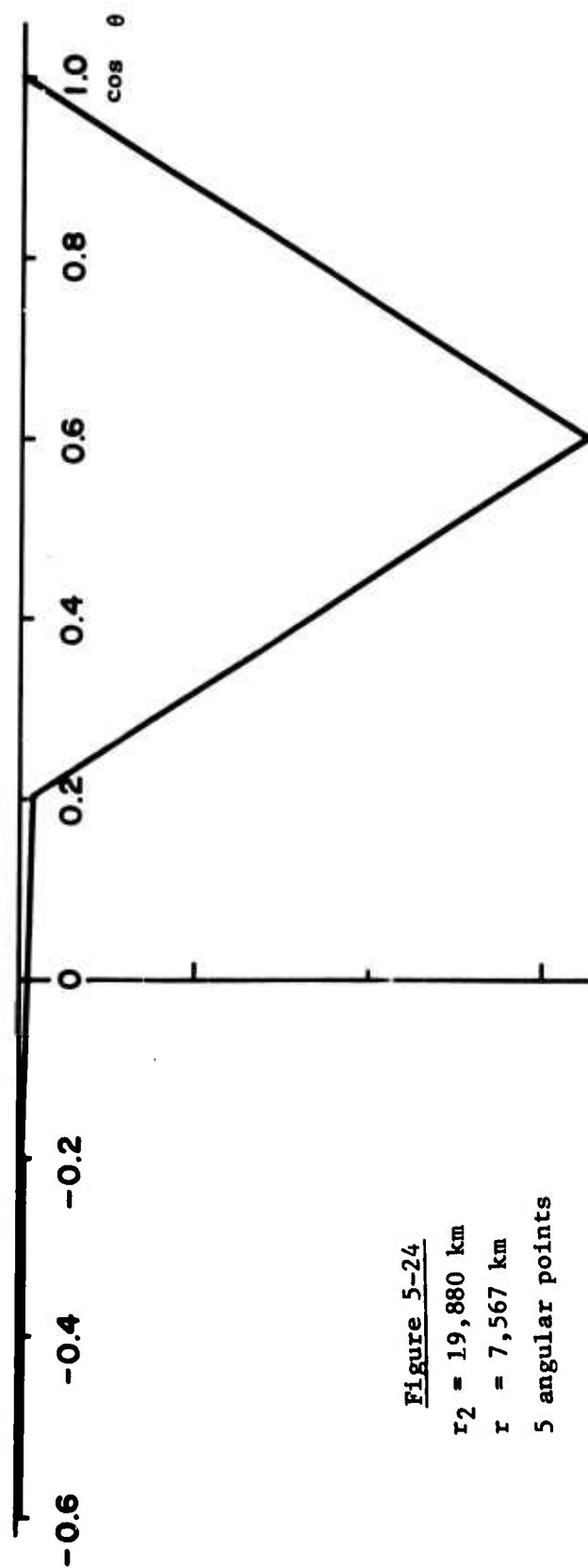Figure 5-23
$r_2 = 8,370$ km
$x = +.6$
1,280 radial points

Figure 5-24

r_2 = 19,880 km

r = 7,567 km
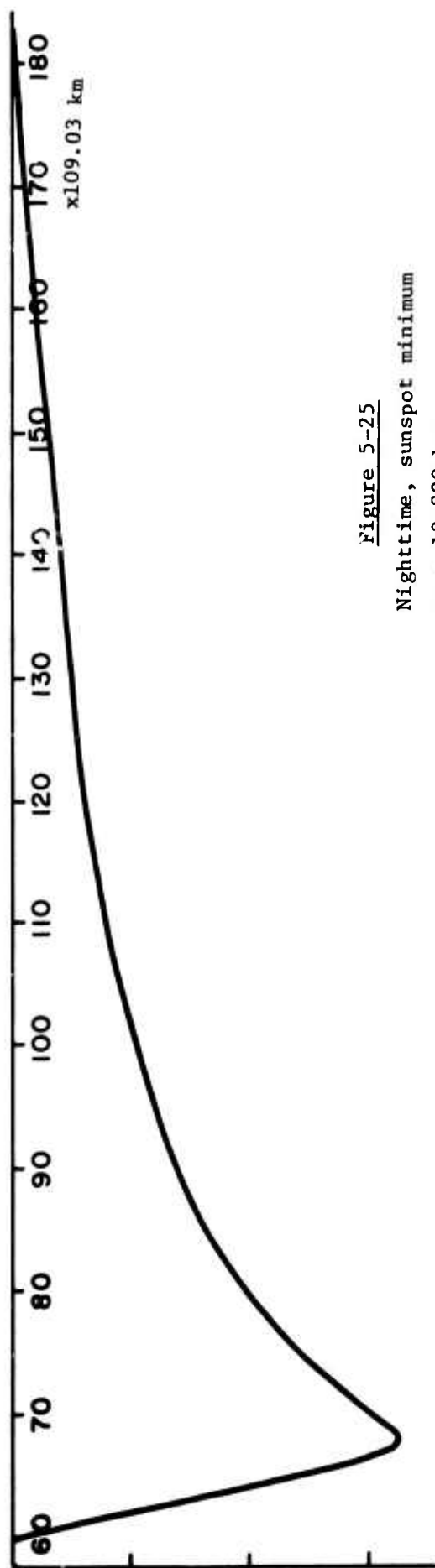
5 angular points

Figure 5-25

Nighttime, sunspot minimum

$r_2 = 19,880$ km

$x = +.6$

640 radial points

x109.03 km
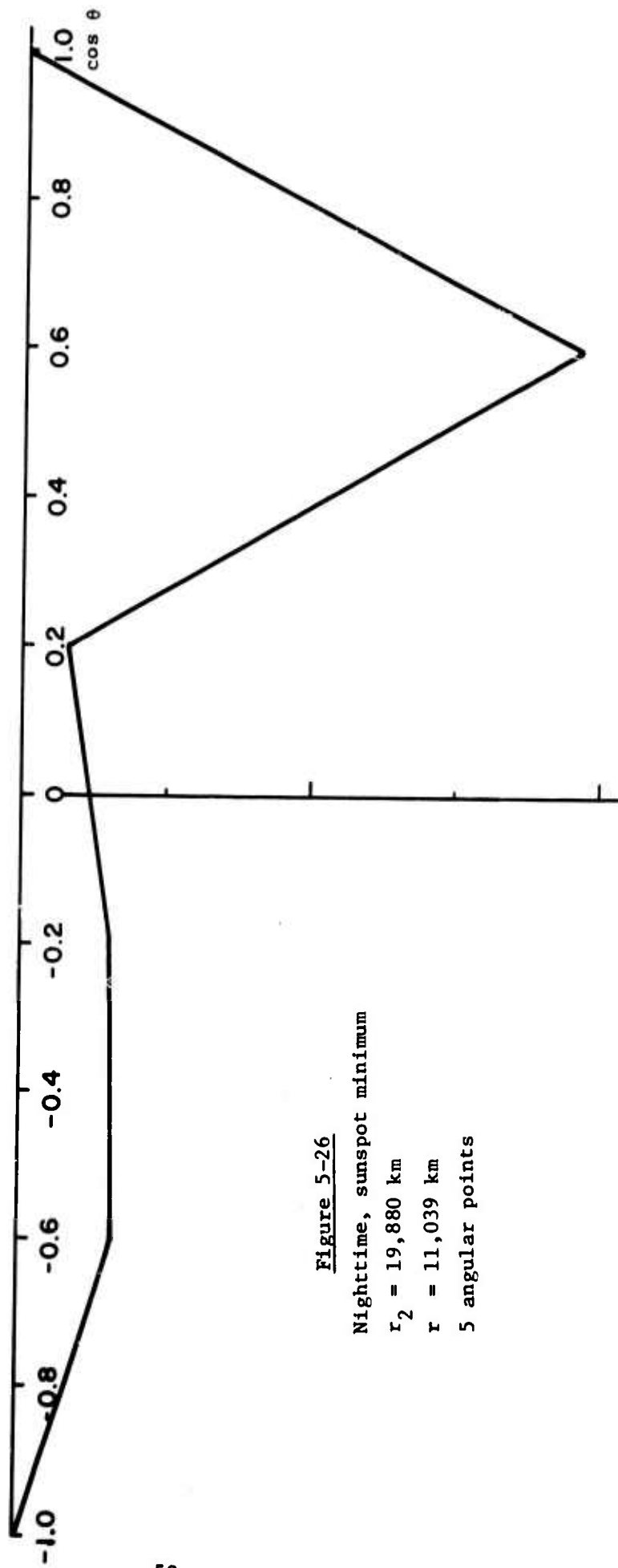
Figure 5-26

Nighttime, sunspot minimum
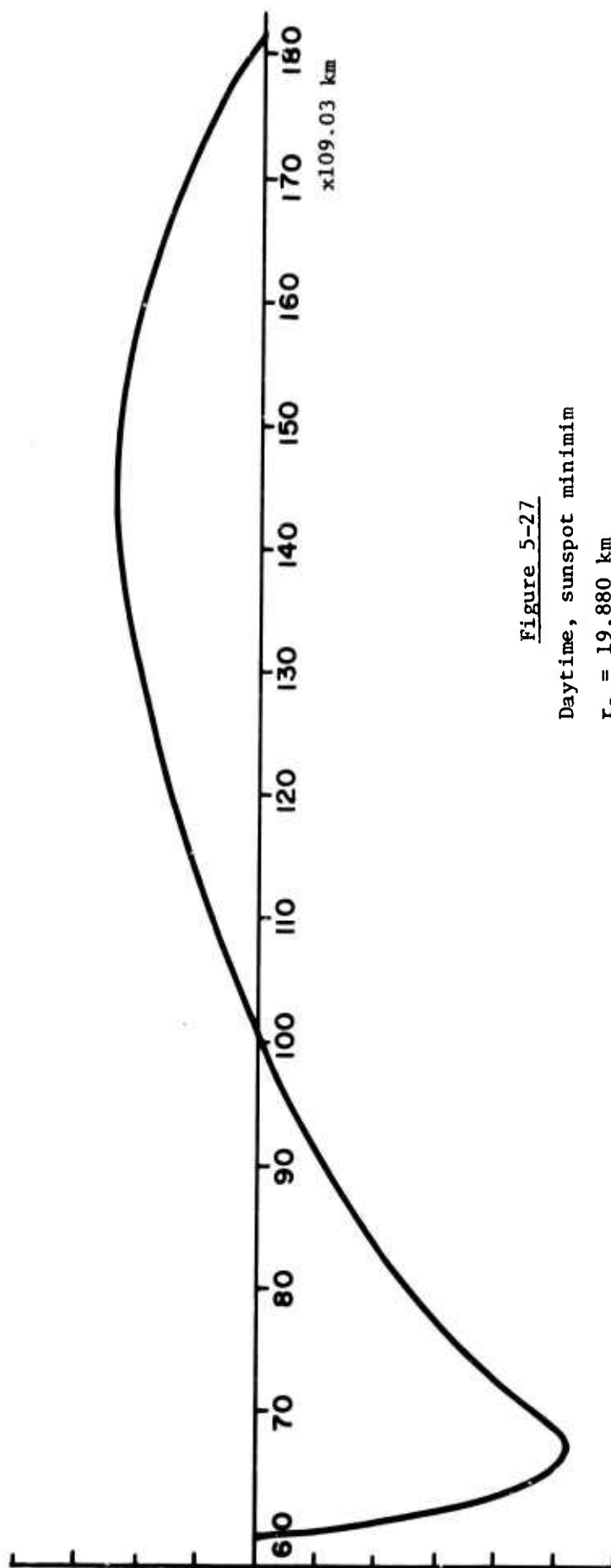
$r_2 = 19,880$ km

$r = 11,039$ km

5 angular points

Figure 5-27

Daytime, sunspot minimim

r_2 = 19,880 km
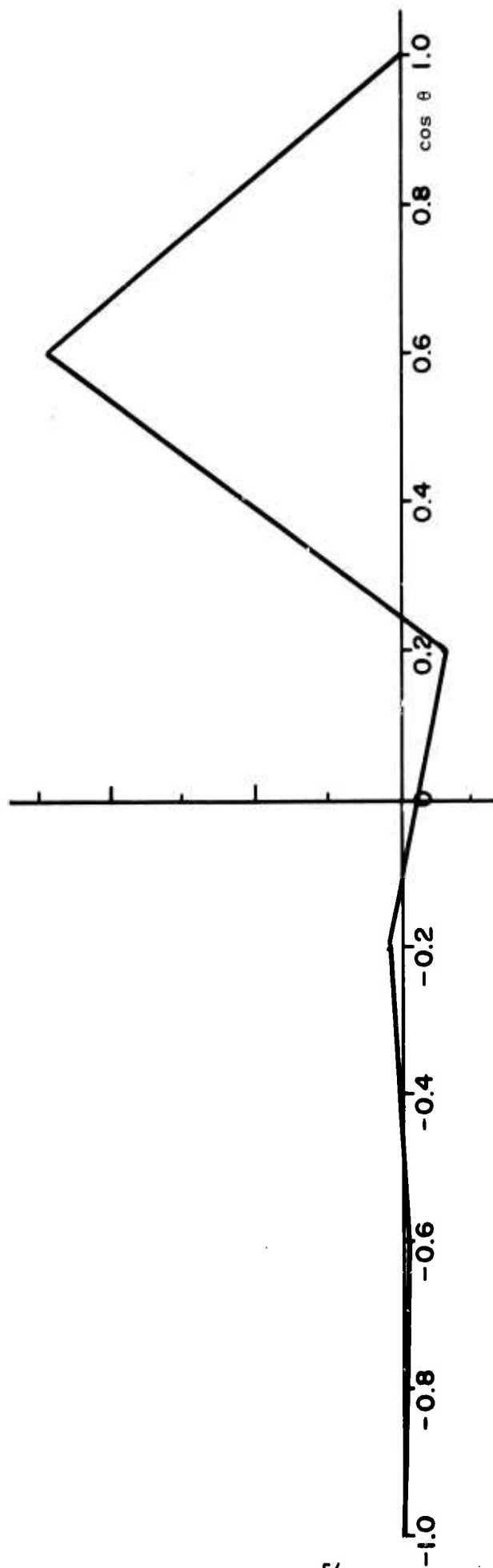
x = +.6

640 radial points

Figure 5-28

Daytime, sunspot minimum

r_2 = 19,880 km

r = 11,029 km

5 angular points

6. Conclusion

This report has described the successful development of a computer program for solving the poloidal (unguided) magnetohydrodynamic wave equation. The solution to this problem is very closely related to the determination of the field amplitudes in the complex asymmetric model describing the real ionosphere. The reason for this is that recent developments have shown that neither the toroidal (guided) mode nor the highly asymmetric poloidal modes are viable in a dipole magnetic field.

We have investigated the credibility of this computer program by comparing numerical results with analytic results, where possible, and with the results of a different computational method.

Thus far, there has not appeared to be any intrinsic difficulty in incorporating features o_ the real ionosphere into the model although we have not begun to explore asymmetric situations, such as the day-night asymmetry.

6. Conclusion

This report has described the successful development of a computer program for solving the poloidal (unguided) magnetohydrodynamic wave equation. The solution to this problem is very closely related to the determination of the field amplitudes in the complex asymmetric model describing the real ionosphere. The reason for this is that recent developments have shown that neither the toroidal (guided) mode nor the highly asymmetric poloidal modes are viable in a dipole magnetic field.

We have investigated the credibility of this computer program by comparing numerical results with analytic results, where possible, and with the results of a different computational method.

Thus far, there has not appeared to be any intrinsic difficulty in incorporating features of the real ionosphere into the model although we have not begun to explore asymmetric situations, such as the day-night asymmetry.

APPENDIX

TWO-POINT BOUNDARY PROBLEM

The two-point boundary problem may be stated as follows:
For a second order differential equation $L\,y(x) = S$ where $y(x)$ is
the unknown function, L is a differential operator and S is an
inhomogeneous term, the boundary conditions are that $f_1(y(x_a))$ and
$f_2(y(x_b))$ are specified where f_1 and f_2 are arbitrary functions or
operators. The simplest boundary conditions of this type, which are
the ones we are actually concerned with, are $y(x_a)=0$ and $y(x_b)=0$.
These conditions would apply, for example, to a stretched string
which is held fixed at two points, x_a and x_b, under a driving force
S. If the driving force is not present, then such a problem has a
non-trivial solution only when a specified parameter has certain
fixed values, i.e., eigenvalues. When there is a driving term a
solution usually exists for any value of the specified parameter.
However, the solution is usually largest when the parameter equals
one of the eigenvalues (i.e. resonance occurs). Since we have a
driving term, the problem is not to determine the eigenvalues and
eigenfunctions, but rather to solve $Ly=S$ for y subject to the two-
point boundary conditions.

In order to solve the equation numerically, there are two
standard methods: (1) Total solution method; (2) Shooting method.

1. Total Solution Method

In the total solution method, the differential equation is
differenced at a set of grid points including the endpoints so that
the boundary conditions are incorporated directly into the difference
equations. The set of coupled equations leads to a problem of solv-
ing a set of linear equations involving a sparsely populated matrix

whose order is equal to the number of grid points. For good accuracy (small truncation error) this may involve using a large number of points. This method was used in the case where the partial differential equation (4-4) was differenced in two dimensions. It has several advantages over the method used below, but unfortunately, as of this writing we could not get the program to run on the IBM 7094 although it had been working on the CDC 6400. (There seem to be some limitations in the former machine which do not exist in the latter.)

2. Shooting Method

Assuming that $y(x_a)$ is given, it is necessary to know $y'(x_a)$ in order to start the numerical integration. In the shooting method a value for $y'(x_a)$ is guessed and the integration is performed. Then the value $y(x_b)$, if this is given as the boundary condition at x_b, would be compared with the value $y(x_b)$ computed on the basis of the assumed value of $y'(x_a)$. A second integration would be performed with a different value of $y'(x_a)$. By suitably choosing $y'(x_a)$ the solution can be made to assume the value $y(x_b)$ specified by the boundary conditions.

This method has several disadvantages: (1) It is not an exact method. Several integrations must be performed before a satisfactory value for $y'(x_a)$ is found, that is, before a solution is found whose value $y(x_b)$ is within a prescribed tolerance. Also, and probably more significant, if there is any tendency toward instability, it will be exhibited when the equation is being integrated for incorrect values of $y'(x_a)$.

In spite of these difficulties it is the second method, the shooting method, which has been used successfully in the present case.

-57-

For the case when Eq. (4-4) is to be solved, this is equivalent to solving 2N-2 first order differential equations

$$\frac{dy_i(x)}{dx} = f_i\left(y_1, y_2, \; y_i, \; y_{2N-2}, x\right) \qquad (A-1)$$

Here the y with odd subscripts are the amplitudes and y with even subscripts are the derivatives. The boundary conditions are that $y_i(x_a)=0$ and $y_i(x_b)=0$ for i odd. The assumed values for $y_{2i}(x_a)$ are denoted by η_i. Since the set $\{\eta_i\}$ is chosen anew for each integration, this will be denoted by a superscript, i.e. $\eta_i^{(j)}$ where $1 < j < N$. The actual values achieved for $y_{2i-1}(x_b)$ when $\eta_i^{(j)}$ are used as imputs are denoted by $\xi_i^{(j)}$. The assumption is made that

$$\xi_i = \sum_{k} a_{ik}\eta_k + b_i \qquad (A-2)$$

where a_{ik} and b_i are constants. That is, it is assumed that there is a linear relationship between the set $\{\eta_k\}$ and the set $\{\xi_i\}$. Then we have, using the quantities $\xi_i^{(j)}$, found by integrating the differential equations

$$\xi_i^{(j)} = \sum_{k=1}^{N-1} a_{ik}\eta_k^{(j)} + b_i \qquad (A-3)$$

Now for each i the N equations (i.e., $1 \leq j \leq N$) are a linear set of equations for the unknowns a_{ik} and b_i. Solving these we find the a_{ik} and b_i so that we have

$$\xi_i = \sum_{k=1}^{N-1} a_{ik} \eta_k + b_i \tag{A-4}$$

If we now set $\xi_i = 0$ as demanded by the condition $y_i(x_b) = 0$ (i odd), then the η_k are determined by solving

$$\sum_{k=1}^{N-1} a_{ik} \eta_k = -b_i \tag{A-5}$$

This gives a new set of η_i from which to start the integration and this leads to a new set of ξ_i.

The next step in the method is to test the ξ_i to see if they are within acceptable bounds. If so, the solution has been found. If not, a new calculation is performed for a_{ik} and b_i using the sets of $\{\xi_i\}$ and $\{\eta_i\}$ for $2 \leq j \leq N+1$. From this a new set of η_i are predicted, integration of the equations performed and the new ξ_i are tested. This process, in theory, continues until an acceptable solution is reached. In practice, it has been found impossible to make the individual ξ_i less than about 10^{-6} of the derivatives at the end point. This is related to the fact that the function and its derivative are related quantities and that there are about 8 significant figures held on the IBM machine. When calculations were performed on a CDC machine which held more significant figures for each number, the convergence was improved.

One interesting facet of this technique is related to a view in which the (η_i) are considered imputs to a system (of differential equations) for which (ξ_i) are the outputs. In order to solve (A-3) for a_{ik} we must deal with the matrix $\eta_k^{(j)}$ of imputs which we are free to choose.

Since the matrix is not to be ill-conditioned or singular we require that the numbers $\eta_k^{(j)}$ not be chosen in any simply-related manner because in that case the matrix would be singular or close to it. In particular, we have chosen the elements of $\eta_k^{(j)}$ to be random, so that the method used here to sclve the differential equation-two point boundary problem-may be viewed as equivalent to exploring a system by means of observing its response to random imputs.

B. EXPERIMENTAL STUDY OF ION-ACOUSTIC WAVE PROPAGATION

1. Introduction

One of the problems in the magnetic detection of a high
altitude nuclear detonation is in predicting the propagation of the
wave signal through the lower ionosphere where the plasma and neutral
density vary rapidly with altitude. The problem is particularly
difficult for an analytical approach because the plasma model varies in
this region from a collisionless, fully ionized plasma to that of a
collision-dominated, weakly ionized gas. The wave signal which
propagates through this region is attenuated by collisions with the
neutrals. Such collisional effect couples the plasma wave motion
into the neutrals, and the coupling is strong when the collision
frequency becomes comparable with the wave frequency. Existing
theoretical studies on the problem are based on various simplifying
models. The validity of these models can only be assessed by
laboratory experiments under controlled conditions.

The laboratory technique for studying the phenomena of
interest has been discussed in a previous report[6]. Efforts during
the current reporting period have been directed toward construction
of the experimental apparatus, instrumentation, and experimental
planning. This work is reported in the following sections.

2. Construction of the Experimental Apparatus

It was determined that the experiment can best be carried out in an alkaline plasma generator operating in the vapor pressure mode. In order to generate such a plasma, several pieces of equipment are needed. These include a vacuum manifold and associated pumping network, a temperature regulated cesium reservoir for maintaining the cesium vapor pressure, an oven to maintain the entire assembly at an elevated temperature, and, finally, an electron bombardment heating system for heating the ionizing hot plate. The design and construction of the equipment are described in the following sections.

A. Vacuum Manifold

The vacuum manifold serves to confine the alkaline metal vapor in a controlled environment. The vacuum system is shown schematically in Fig. 1. The system consists of a cylindrical vacuum manifold 20 cm in diameter by 100 cm in length, enclosed by blank flanges on each end. Metal gaskets are used throughout to insure high temperature operation of the system. A pumping duct is connected to the system through one of the flanges. The system can be isolated from the pumps during the experiment by the bakeable Granville-Phillips type 267 Auroseal valve. This valve was chosen because of its ability to operate at elevated temperatures, both in the open and closed positions. A cold trap is inserted in the pumping line to condense out the room temperature cesium vapor, which can attack the pumps and also present a health hazard. When the system is isolated from the pumping network after initial pump down, cesium vapor is introduced into the system by heating up the reservoir, which is connected to the system via a Tee in the pumping duct. The temperature of the reservoir is controlled by a heating element imbedded
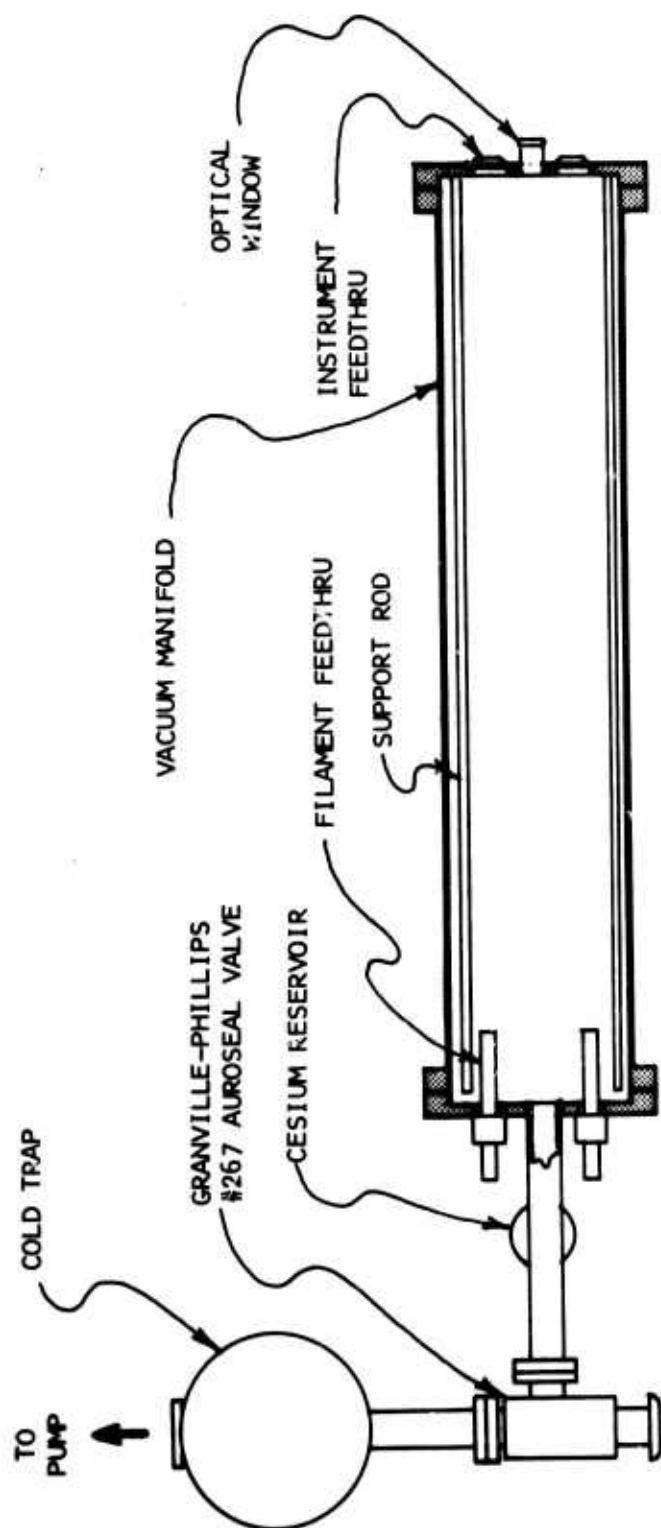
Figure 1. Vacuum System Assembly

in an insulating jacket surrounding it. The flanges are equipped
with vacuum feedthru elements for power and signal connections into
the plasma. A view of the vacuum system assembly is shown in the
photograph in Fig. 2.

B. Oven Assembly

In order to avoid the condensation of the cesium vapor,
it is necessary to maintain the entire system at an elevated tempera-
ture. It was originally intended that the entire system be maintained
in an oven heated by the hot plate. However, later heat transfer
calculations have shown that, because of the large heat flux escaping
from the source, it would be desirable to cool the regions directly
heated by the source to avoid excess heating and separately heat the
pumping ducts and the bakeable valve by external heating elements.
Thus, the final design consists of thermally insulated pumping ducts
and valve with imbedded heating elements similar to the cesium
reservoir, and the entire system is installed on a rack to which
cooling fans can be directed to provide cooling desired.

C. Electron Bombardment Heating System

The cesium plasma is to be generated by surface ionization
of the incoming neutrals. In order to maintain charge neutrality,
electrons must be evaporated off as rapidly as ionization takes place.
The electrons are to be generated by thermionic emission. The
temperature of the hot plate required to maintain equal electron
emission and ionization is shown in Fig. 3 as a function of neutral
temperature for cesium on tungsten.

To assure that the plasma sees only a well defined equi-
potential surface, it is desirable that the hot plate be indirectly
heated. Electron bombardment heating is ideally suited for that

VACUUM MANIFOLD

VACUUM GAUGE

COLD TRAP

FILAMENT FEEDTHRU
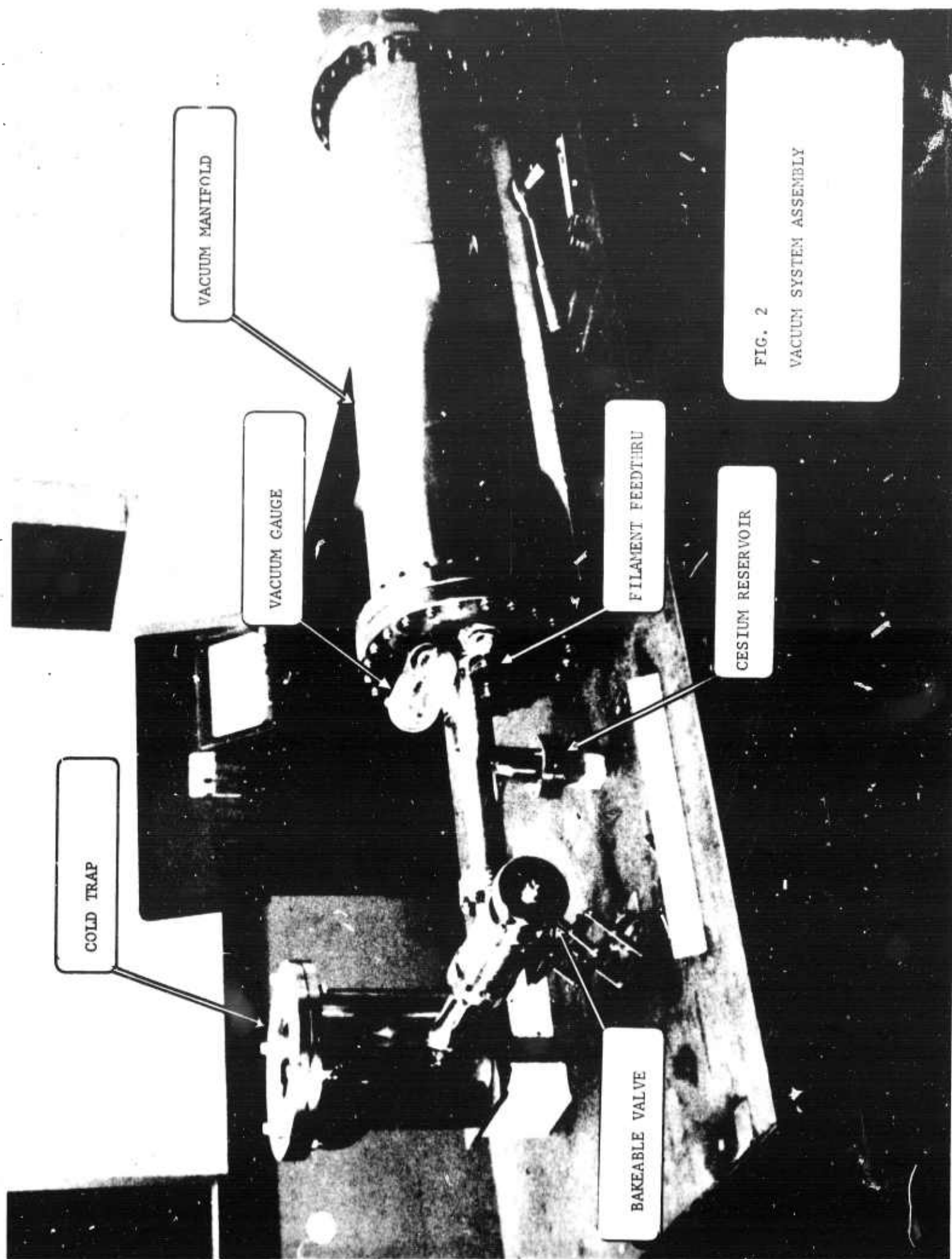
CESIUM RESERVOIR

BAKEABLE VALVE
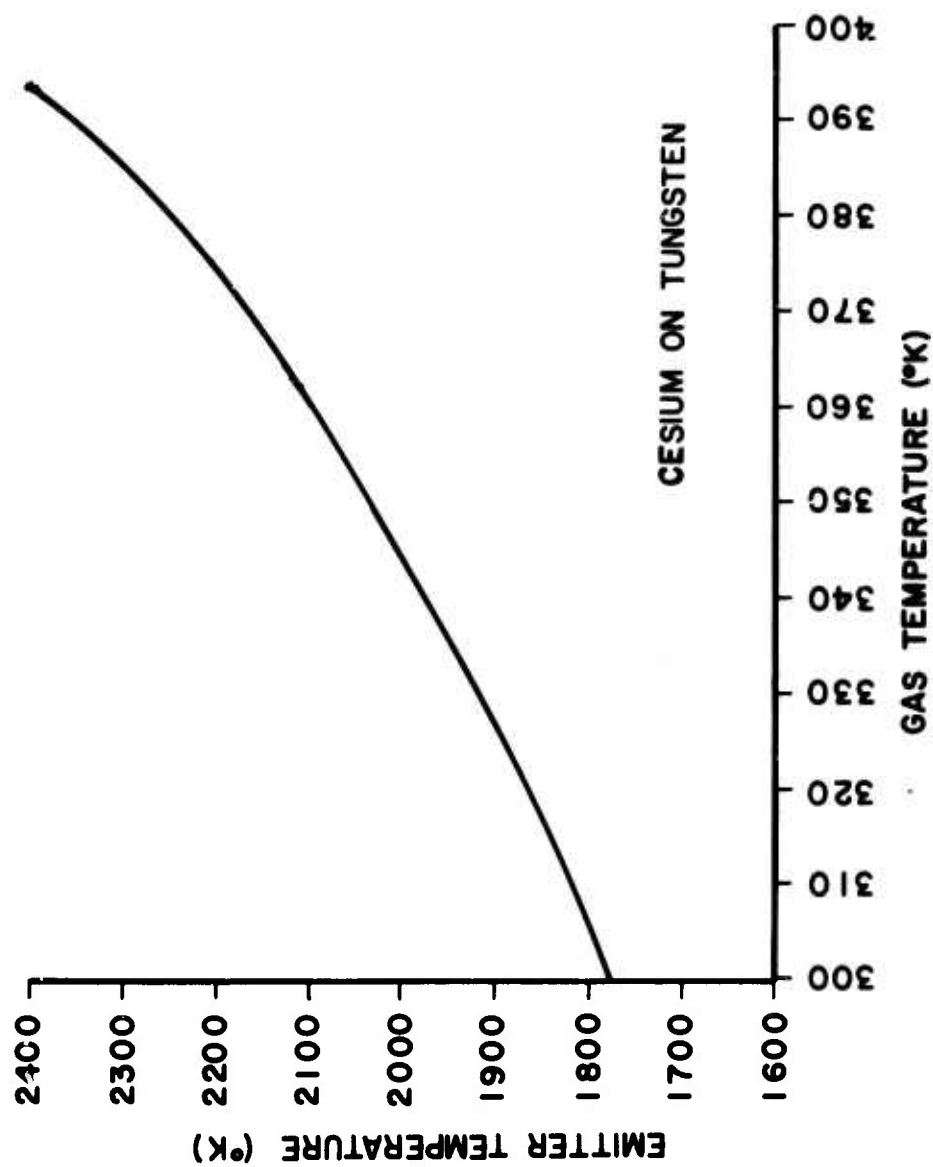
FIG. 2

VACUUM SYSTEM ASSEMBLY

Figure 3. Hot Plate Operating Temperature Reference Chart

purpose. In order to generate a plasma of sufficient volume, it was determined that a surface area of 5 cm^2 would be required. A zig-zag filament covering a circular area of 10 cm diameter was formed with tungsten powder. The filament is to be heated by a 10-volt, 200-amp, current regulated power supply. The filament is biased at -5000 volts, and, thus, the thermionically emitted electrons are accelerated to the tungsten hot plate where the kinetic energy is dissipated in heating up the plate. In order to attain uniform temperature on the surface of the hot plate, a relatively heavy plate of 1 cm thickness was used.

To heat the plate to a high temperature, a rather substantial power supply with good regulation characteristics is required to maintain operational stability. The high current required to heat the filament and the high voltage required to accelerate the electrons are incorporated into a single-unit design which produces a maximum current stabilized supply of 200 amps at 10 volts, or 100 amps at 20 volts to the filament biased at -5000 volts. The high voltage supply is voltage regulated and continuously variable from 500 to 5000 volts with a maximum output of 1.5 amps. The construction of the power supply has been completed and the unit is now operational.

The three items discussed above represent the major equipment required for the experiment, and construction of all of these items has been completed.

purpose. In order to generate a plasma of sufficient volume, it was determined that a surface area of 5 cm^2 would be required. A zig-zag filament covering a circular area of 10 cm diameter was formed with tungsten powder. The filament is to be heated by a 10-volt, 200-amp, current regulated power supply. The filament is biased at -5000 volts, and, thus, the thermionically emitted electrons are accelerated to the tungsten hot plate where the kinetic energy is dissipated in heating up the plate. In order to attain uniform temperature on the surface of the hot plate, a relatively heavy plate of 1 cm thickness was used.

To heat the plate to a high temperature, a rather substantial power supply with good regulation characteristics is required to maintain operational stability. The high current required to heat the filament and the high voltage required to accelerate the electrons are incorporated into a single-unit design which produces a maximum current stabilized supply of 200 amps at 10 volts, or 100 amps at 20 volts to the filament biased at -5000 volts. The high voltage supply is voltage regulated and continuously variable from 500 to 5000 volts with a maximum output of 1.5 amps. The construction of the power supply has been completed and the unit is now operational.

The three items discussed above represent the major equipment required for the experiment, and construction of all of these items has been completed.

3. Instrumentation

Current work in the progress of the experiment has been concentrated in instrumentation of the apparatus. This instrumentation includes the installation of the hot plate assembly, diagnostic sensors, and radiation shields. Because the system is to be operated at an elevated temperature, metal gaskets are required for all demountable seals. Therefore, it was decided at an early stage, for economic reasons as well as for simplicity, that all instrumentation is to be installed inside the vacuum manifold with all leads brought out through feedthru elements installed in the end flanges. To support the various electrodes, two rods cantilevered at one of the end flanges run the length of the vacuum manifold. The hot plate assembly, electrostatic probes and grids, thermocouples, and radiation shields are all hung from these two rods. The detail construction of the various parts is described in the following.

A. Hot Plate Assembly

The hot plate consists of a 1 cm thick tungsten circular plate, 10 cm in diameter, mounted in two boron nitride disks as shown in Fig. 4. The boron nitride disks serve as electrical insulation so that the hot plate bias may be varied with respect to ground. The disks are held together by two brackets made from tantalum sheet metal and attached to the supporting rod. The tungsten filament is attached directly onto the high current, high voltage feedthru elements, and the entire assembly is surrounded by radiation shields to cut heat loss. This design differs from the one proposed in the last semi-annual report in greater simplicity and ease of installation.
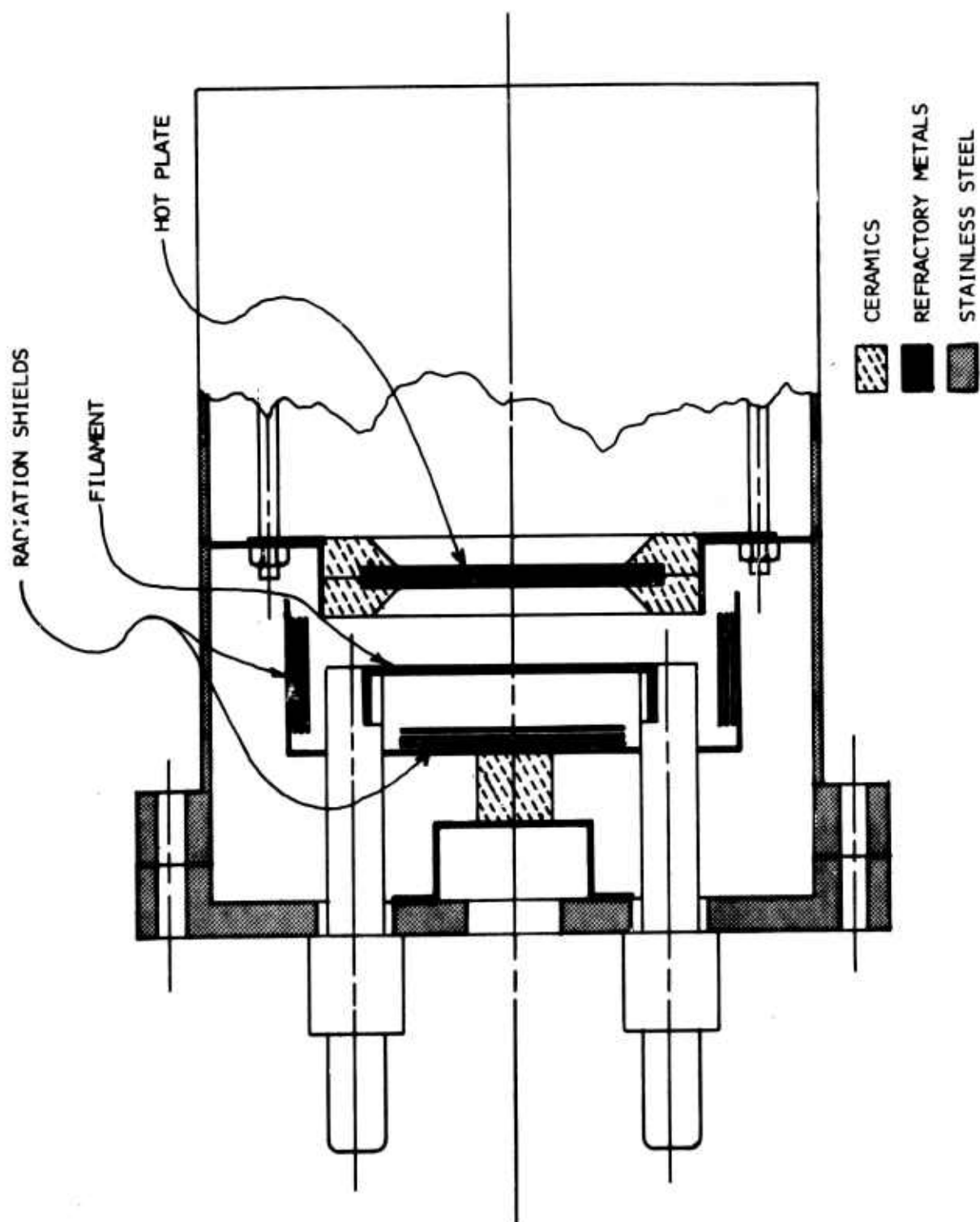
RADIATION SHIELDS

FILAMENT

HOT PLATE

CERAMICS

REFRACTORY METALS

STAINLESS STEEL

Figure 4. Hot Plate Assembly

B.   Diagnostics

The basic instrumentation for the experiment consists of electrostatic probes for measuring spatial distribution of the plasma, grids for excitation and detection of waves, and thermocouples to monitor the temperature in the reservoir and other regions of interest. The probes and grids are fabricated from tungsten wires insulated by alumina tubing and mounted on a specially designed probe holder which will self-center the probe at any radial and axial positions desired. The signals are transmitted by Teflon insulated wires which can withstand temperatures of 500°K.

The temperature of the reservoir is monitored by a thermo-couple attached to the outside metal wall. Since the reservoir is enclosed in heavy insulation, we anticipate the temperature drop across the metal wall will be insignificant, and thus the external temperature measurement will give a satisfactory estimate of the reservoir temperature. The neutral background pressure in the system will be ascertained from the measured temperature of the reservoir and the vapor pressure curve of cesium.

To avoid condensation of the vapor at any point in the system, it is important to assure that the temperature throughout the system is kept above that of the reservoir. Since the only require-ment for temperature in this case is that it should be above a certain value, we have painted the system at various control points with Thermolaq paint rather than actually measuring temperatures at these points. This procedure considerably simplified the monitoring requirements.

C.   Radiation Shields

In order to maintain the hot plate at elevated temperatur with minimum power input, and also to protect the wire insulations

from over heating, it is desirable to minimize the heat transfer from the central regions. Calculations have shown that radiation and free convection are able to remove about 500 watts from the vacuum walls at 500°K. Forced convection can increase this rate, possibly by a factor of two. Therefore, radiant heat transfer from the hot plate must not exceed this value. This can be accomplished by the installation of 10 layers of radiation shields. Present plan calls for the installation of 15 layers of 1 mil thick tantalum foil surrounding a useful volume of about 3 litres. This shield is presently being installed.

The final experimental work can be carried out upon the completion of these various installations in the near future.

4. Experimental Program

The basic objective of the experiment is to study the propagation of ion acoustic waves in a plasma medium where the parameters may be varied under controlled conditions. The basic experimental arrangement is shown schematically in Fig. 5. Longitudinal waves are excited in the plasma by applying a tone burst of a chosen frequency oscillation and detected by sensors along the plasma column. A tone burst signal is preferred over a CW signal so that directly coupled signals can readily be distinguished from the ion wave signals.

The controlled experimental variables are the plasma density n, the neutral density n_o, the wave period τ, the scale length λ, and grid separation d_2. The experimentally measurable parameters of interest are the time delay τ_1 and τ_2 of the signal arriving at detectors 1 and 2 and the amplitude of the received signals A_1 and A_2. From these data one can construct the dispersion relation for the system which, in principle, defines the system completely.

Comparison of the experimentally determined wave propagation characteristics with theoretical predictions can be expected to yield valuable insight into theoretical modelling of waves in inhomogeneous media. The phenomenon of particular interest is the damping of the waves. It is expected that we will be able to observe both collisional and collisionless damping which are manifestations of various coupling mechanisms. The optimal detection method for signals propagating through such a weakly ionized medium can be determined from the experimental conclusions.
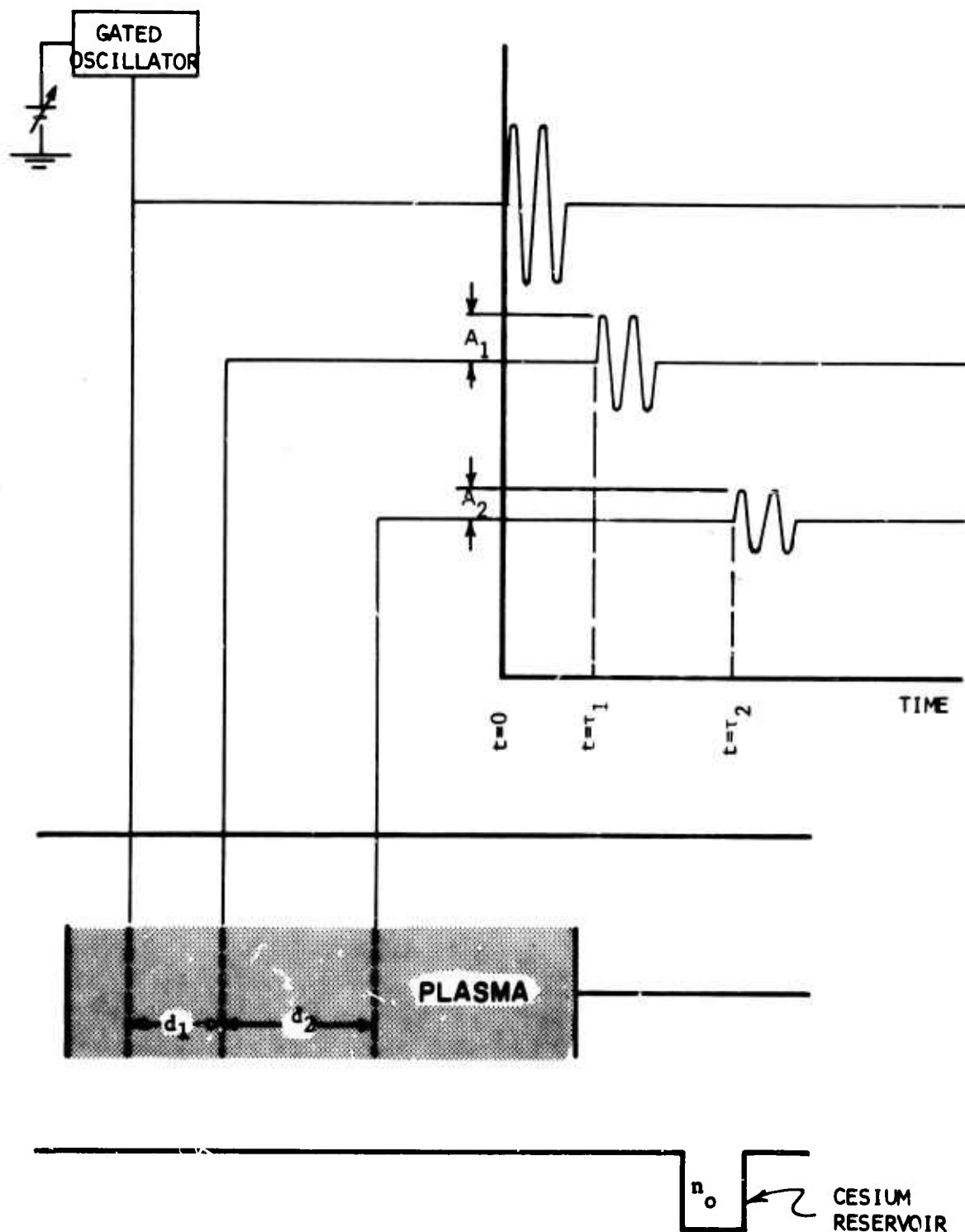
Figure 5. Experimental Scheme

REFERENCES

1. I. S. Berezin and N. P. Zhidkov, <u>Computing Methods</u>, Vol. II Pergamon Press (1965) p. 580

2. H. R. Radoski and R. L. Carovillano, Phys. Fluids $\underline{9}$, 285 (1966)

3. H. Radoski and J. McClay, J. Geoph. Research (to be published)

4. J. Dungey in <u>Geophysics</u>, C. Dewitt, J. Hieblat; A. Lebeau ed, Gordon and Breach (1963)

5. H. Radoski, J. Geoph. Research $\underline{72}$, 4026 (1967)

6. B. L. Murphy, <u>et al.</u> , <u>Theoretical Study of Magnetohydrodynamic Wave Propagation and Experimental Study of Collisional Effects on Wave Propagation</u>, Semi-Annual Report, Mt. Auburn Research Associates, Inc., 23 March 1967.

7. W. Magnus, F. Oberhettinger, <u>Functions of Mathematical Physics</u>, Chelsea Publishing Company (1954), p. 73

8. R. J. Greenfield, "Two Dimensional Calculations of Magnetic Micropulsation Resonances," M.I.T. Thesis (1965)

9. C. W. Chapman and F. X. Bostick, Jr., "A Study of the Application of Finite-Difference Techniques to ULF Waves in a Spherical Model Inhomogeneous, Anisotropic, Atmospheric Plasma", University of Texas Electrical Engineering Research Laboratory Report No. 141 (1966)

10. C. E. Prince and F. X. Bostick, Jr., J. Geoph. Research, $\underline{69}$, 3213, 1964